M 2018

U.PORTO
FEUP FACULDADE DE ENGENHARIA
UNIVERSIDADE DO PORTO

STRUCTURED METAL-FREE CARBON MATERIALS FOR PHOTOCATALYTIC WASTEWATER TREATMENT

ANDRÉ TIAGO TORRES PINTO
DISSERTAÇÃO DE MESTRADO APRESENTADA
À FACULDADE DE ENGENHARIA DA UNIVERSIDADE DO PORTO EM
ENGENHARIA QUÍMICA

Master in Chemical Engineering

Structured metal-free carbon materials for photocatalytic wastewater treatment

A Master's dissertation

of

André Tiago Torres Pinto

Developed within the course of Dissertation

held in

Laboratory of Separation and Reaction Engineering - Laboratory of Catalysis and Materials

SRE CM
ASSOCIATE LABORATORY
LABORATORY OF SEPARATION AND REACTION ENGINEERING
LABORATORY OF CATALYSIS AND MATERIALS

Supervisors:

Professor Adrián M. T. Silva

Doctor Cláudia G. Silva

Professor Joaquim L. Faria

U.PORTO
FEUP FACULDADE DE ENGENHARIA
UNIVERSIDADE DO PORTO

Departamento de Engenharia Química

July of 2018

Agradecimentos

O esforço e a dedicação não seriam suficientes para a realização desta dissertação sem o apoio e o incentivo de algumas pessoas às quais tenho de agradecer.

Em primeiro lugar, ao Professor Adrián Silva, o meu orientador, por toda a preocupação, disponibilidade e dedicação que demonstrou nos últimos meses e por todas as oportunidades que me ofereceu. Aos meus coorientadores Doutora Cláudia Silva por toda a ajuda que me deu e pela atenção que sempre disponibilizou e ao Professor Joaquim Luís Faria por todos os conhecimentos transmitidos.

À Doutora Maria José Sampaio por estar sempre presente, por todos os conselhos e por ter partilhado comigo muito mais do que conhecimento científico.

Ao Laboratório Associado LSRE-LCM pela disponibilização dos seus espaços e recursos.

À Professora Madalena Dias e à Andreia Ribeiro pela disponibilização do equipamento para medição de potencial zeta. E à Liliana Pereira pela ajuda nas medições de carbono orgânico total.

À Raquel Fernandes e à Joana Lopes pelo apoio em todos os momentos. Aos meus restantes colegas de laboratório pela ajuda e pela boa disposição todos os dias.

À Joana, à Raquel, ao Pedro, à Beatriz e à Cristina pela amizade e presença constante.

Finalmente, à minha mãe, ao meu pai e à minha irmã pelo apoio incondicional, e ao meu sobrinho que me incentiva a ir trabalhar todos os dias.

Este trabalho foi desenvolvido no âmbito do projeto "AIProcMat@N2020 - Advanced Industrial Processes and Materials for a Sustainable Northern Region of Portugal 2020", com referência NORTE-01-0145-FEDER-000006, cofinanciado pelo Programa Operacional Regional do Norte (NORTE 2020), através do Portugal 2020 e do Fundo Europeu de Desenvolvimento Regional (FEDER), do projeto POCI-01-0145-FEDER-006984 - Laboratório Associado LSRE-LCM - financiado pelo FEDER, através do COMPETE2020 – Programa Operacional Competitividade e Internacionalização (POCI) e por fundos nacionais através da FCT - Fundação para a Ciência e a Tecnologia I.P., e do projeto NORTE-01-0145-FEDER-031049, financiado pelo FEDER, através do Programa NORTE 2020 e com o apoio financeiro da FCT/MCTES através de fundos nacionais (PIDDAC).

Abstract

Advanced oxidation processes are conceptually based on the production of highly reactive species, which can oxidize organic molecules. Among these processes, heterogeneous photocatalysis employs ultraviolet and/or visible radiation as driving force. Several photocatalysts have been studied, but metal-free graphitic carbon nitride has recently attracted a huge interest since it can be easily synthesized, is active under visible light radiation and efficiently removes organic pollutants from water. Moreover, in certain conditions, i.e. with an oxygen gas feed, hydrogen peroxide (H_2O_2) can be both generated and decomposed to hydroxyl radicals, which can improve the performance of the process. However, most of reported studies have employed dyes as model compounds and the respective mechanisms of pollutant degradation and H_2O_2 formation are not yet well understood.

The main aim of the present study was to expand the knowledge on the mechanisms involved in this photocatalytic system, using phenol as probe molecule, and to compare the degradation of different aromatic pollutants. To this end, a metal-free thermally exfoliated graphitic carbon nitride material (gCN_T) was used. The photocatalytic experiments were carried out with light emitting diodes as irradiation source (maximum emission wavelength at 417 nm) and different operating conditions. The pollutant and H_2O_2 concentrations, as well as the total organic carbon content, were determined during the experiments using different analytical techniques.

It was demonstrated that H_2O_2 is formed and its concentration increases in the presence of photoactivated gCN_T, oxygen and a given compound acting as proton donor (e.g., one of the aromatic compounds tested as model pollutant). In the absence of the proton donor, H_2O_2 decomposes with photoactivated gCN_T, its concentration decreasing even when oxygen is not present. The experiments with different aromatic pollutants allowed to conclude about the effect on the degradation rate of the aromatic ring substituents. Most of these compounds were removed to levels below the limit of quantification in less than 3 h of irradiation. Additionally, the highest amount of H_2O_2 achieved in the present dissertation was considerably superior to those found in the literature with this type of metal-free photocatalysts. Therefore, the studied gCN_T material is a remarkable photocatalyst for the degradation of organic pollutants as well as for H_2O_2 production.

Keywords: photocatalysis; graphitic carbon nitride; pollutant degradation; aromatic compounds; mechanisms; hydrogen peroxide generation.

Resumo

Os processos avançados de oxidação consistem na produção de espécies altamente reativas capazes de oxidar moléculas orgânicas. Entre estes processos, a fotocatálise heterogénea utiliza radiação ultravioleta e/ou visível como força motriz. Há estudos publicados com vários fotocatalisadores, no entanto, o interesse pelo nitreto de carbono grafítico tem aumentado recentemente, uma vez que este material pode ser facilmente sintetizado, ativado com luz visível e remover eficientemente compostos orgânicos presentes na água. Além disso, em certas condições, como na presença de uma corrente de oxigénio, pode haver formação de peróxido de hidrogénio (H_2O_2) e posterior decomposição em radicais hidroxilo, que podem melhorar o desempenho do processo. No entanto, a maioria dos estudos publicados utilizam corantes como compostos modelo e os respetivos mecanismos de degradação de poluentes e de formação de H_2O_2 não são ainda bem conhecidos.

O principal objetivo deste estudo é ampliar o conhecimento sobre os mecanismos envolvidos neste sistema fotocatalítico, utilizando o fenol como composto modelo, e comparando a degradação de vários compostos aromáticos. Para tal, foi utilizado um material de nitreto de carbono grafítico termicamente exfoliado e livre de metais (gCN_T). As experiências fotocatalíticas foram realizadas usando díodos emissores de luz (LEDs) como fonte de irradiação (comprimento de onda de emissão máxima de 417 nm) e testando várias condições operatórias. As concentrações de poluente e de H_2O_2, bem como de carbono orgânico total, foram determinadas durante os ensaios experimentais.

Foi demonstrada a formação de H_2O_2 e que a sua concentração aumenta na presença de gCN_T foto-ativado, oxigénio e um composto dador de protões (como, por exemplo, um dos compostos aromáticos estudados). Na ausência de um dador de protões, o H_2O_2 decompõe-se na presença de gCN_T foto-ativado, a sua concentração diminuindo mesmo quando não existe oxigénio dissolvido no sistema. Os estudos efetuados com outros poluentes aromáticos permitiram compreender o efeito dos grupos substituintes no anel aromático na velocidade de degradação. Em menos de 3 h de irradiação, a maioria dos compostos estudados foram degradados até concentrações abaixo do limite de quantificação. Adicionalmente, foram obtidas quantidades de H_2O_2 consideravelmente superiores às reportadas na literatura com este tipo de fotocatalisadores livres de metais. Por conseguinte, o material gCN_T estudado apresenta uma elevada atividade fotocatalítica para a degradação de poluentes orgânicos, assim como para a produção de H_2O_2.

Palavras-chave: fotocatálise; nitreto de carbono grafítico; degradação de poluentes; compostos aromáticos; mecanismos; produção de peróxido de hidrogénio.

Declaration

I hereby declare, on my word of honour, that this work is original and that all non-original contributions were properly referenced with source identification.

Porto, 19 july 2018

André Tiago Tomes Pinto

Index

List of Figures

*The marked figures were used without change from the referred works.

List of Tables

Notation and Glossary

List of Symbols

C	Concentration	mol L^{-1}
E_g	Energy band level	eV
K	Kinetic constant	min^{-1}
R	Rate of reaction	mol L^{-1} min^{-1}
T	Temperature	ºC
t	Time	s
λ	Wavelength	nm
ζ	Zeta potential	mV

Indexes

app	Apparent
max	Maximum

List of Acronyms

AOP	Advanced oxidation process
BA	Benzoic acid
BQ	Benzoquinone
CAF	Caffeine
CB	Conduction band
CT	Catechol
DO	Dissolved oxygen
DRUV-vis	Diffuse reflectance ultraviolet-visible
e^-	Electron
GA	Gallic acid
g-C_3N_4	Graphitic carbon nitride
gCN	Bulk graphitic carbon nitride
gCN_T	Thermally exfoliated graphitic carbon nitride
h^+	Photoactivated hole
HBA	4-Hydroxybenzoic acid
$HO^\bullet$	Hydroxyl radical
H_2O_2	Hydrogen peroxide
HPLC	High performance liquid chromatography
HQ	Hydroquinone
LED	Light-emitting diode
MOP	4-Methoxyphenol
O_2	Oxygen
$O_2^{\bullet-}$	Superoxide radical
PCA	Protocatechuic acid
PhOH	Phenol
PZC	Point of zero charge
RC	Resorcinol
ROS	Reactive oxygen species
SEM	Scanning electron microscopy
TOC	Total organic carbon
TYR	Tyrosol
UP H_2O	Ultrapure water
UV-vis	Ultraviolet-visible

1 Introduction

1.1 Presentation of the work

The development of efficient and inexpensive technologies for wastewater treatment is important in the field of environmental protection. Aromatic compounds are present in many industrial wastewaters, and research is being done towards advanced oxidation processes (AOPs), such as visible-light-driven photocatalysis, for the degradation of these pollutants. Sunlight is a free and limitless supply of energy whose radiation works as driving force for the activation of several photocatalysts. To pursue this further, it is proposed in the present study a clean heterogeneous photocatalytic method, using visible light and an optical active metal-free carbon material. In particular, a thermally-treated graphitic carbon nitride (g-C_3N_4), designated as gCN_T, is photoactivated with light-emitting diodes (LEDs) leading to the formation of reactive oxygen species (ROS) which rapidly mineralize the organic pollutants. g-C_3N_4 is synthesized through a simple thermal treatment using cheap precursors, yielding a material with a broad band-gap which assists the photocatalytic degradation of aromatic compounds under visible light. Another important characteristic of this photocatalytic process is the possibility of producing relatively high concentrations of hydrogen peroxide (H_2O_2) under mild conditions: neutral pH, ambient temperature and aerated solutions.

Photocatalytic experiments were performed for many aromatic compounds typically found in liquid effluents, measuring and analyzing the pollutant removal and the production of H_2O_2, according to the operating conditions. The understanding of the mechanisms involved and the kinetics of the whole system are also innovative points of this study.

1.2 Contributions to the work

The work I have done for this dissertation started after manifesting my research interests to Professor Adrián M.T. Silva, who proposed me to continue the work initiated in the framework of the Master Dissertation “Structured carbon materials for wastewater treatment” by Ana Morgado (2016/2017). In the previous semester, I performed some preliminary experiments related with the photocatalytic degradation of phenol in aqueous solutions, following the procedure employed by Ana Morgado. Then, I prepared the photocatalyst which was first synthesized by Maria José Lima at LSRE-LCM and performed the photocatalytic experiments with the help of Doctor Maria José Sampaio. A systematic

study focused on the degradation of aromatic compounds and simultaneous H_2O_2 production in this metal-free and visible-light-driven photocatalytic system, and targeting a better understanding of the respective mechanisms involved, was not performed before.

1.3 Main objectives

The main objective is to develop a system, using visible light and a metal-free catalyst, to promote the abatement of different aromatic compounds with the simultaneous production of H_2O_2 and to better understand the respective mechanisms of this system. To accomplish this goal, three short-term objectives were proposed: 1) define and optimize the operating conditions using a metal-free photocatalyst and phenol as case study; 2) select different aromatic molecules and study the activity of this photocatalyst; and 3) define and implement a methodology allowing the characterization of the mechanisms involved.

1.4 Organization of the dissertation

This dissertation is divided in six chapters. In the present chapter, a brief introduction about the proposed work is presented. The fundamentals of AOPs and heterogeneous photocatalysis are briefly introduced in Chapter 2, together with general insights regarding the use of g-C_3N_4 for the degradation of aromatic compounds and the production/decomposition of H_2O_2. A literature review concerning g-C_3N_4 as photocatalyst and the respective production of H_2O_2 is included in the same chapter, with more focus on the latter due to the more innovative aspects of this topic. A brief description of the materials and methods is given in Chapter 3. In Chapter 4, the catalyst characterization is shown, as well as the reasons behind the selection of different target pollutants, and the results obtained in the photocatalytic studies. Chapters 5 and 6 deal with the conclusions and the assessment of the work done, respectively.

2 State-of-the-art

2.1 Principles of heterogeneous photocatalysis

AOPs conceptually consist on the production of highly reactive species, such as hydroxyl radicals ($HO^{\bullet}$), which can oxidize organic pollutants [1]. These short-lived radicals are non-selective and very powerful oxidants for the removal of refractory organic compounds from a gas or liquid phase [2]. Other reactive oxygen species (ROS), such as superoxide radicals ($O_2^{\bullet -}$), can be also formed by these processes.

Among the different AOPs, photocatalysis is a process where a substance activated by light modifies the rate of a chemical process [3, 4]. Solar light, as an inexhaustible and free source of activating energy, can be used in photocatalysis, resulting in a green and promising technology. Heterogeneous photocatalysis employs a solid material, the photocatalyst, which when exposed to an appropriate light source can generate electron/hole (e^-/h^+) pairs. These e^-/h^+ pairs arise from the excitation of the electrons present in the valence band (VB) and migrate to the conduction band (CB). The difference between the VB and CB energy levels yield the band-gap energy (E_g) of the material. The excitation of the electrons occurs solely by photons with an energy equal to or greater than the band-gap energy. The main steps involved in heterogeneous photocatalysis [5] are schematized in Figure 1.

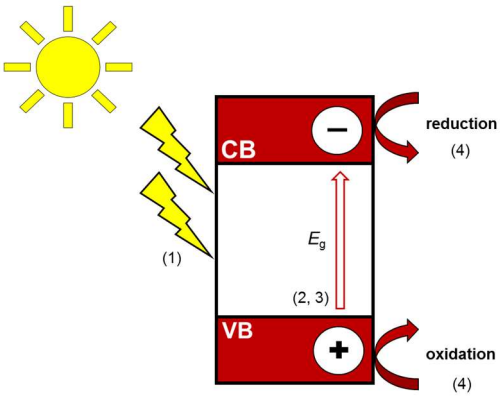

Figure 1. Main steps in heterogeneous photocatalysis: (1) light harvesting; (2) electron excitation and charge separation; (3) electron migration and electron/hole pairs recombination; and (4) charge utilization via surface reduction or oxidation reactions.

The selection of the photocatalyst greatly depends on the VB and CB energy levels and respective band-gap energy. Depending on the band positions, Figure 2 shows several possible photocatalysts and their potential applications, for instance in the degradation of pollutants, carbon dioxide (CO_2) reduction and hydrogen (H_2) or oxygen (O_2)

production [5]. Titanium dioxide (TiO_2) has been the most widely employed photocatalyst for the degradation of water pollutants.

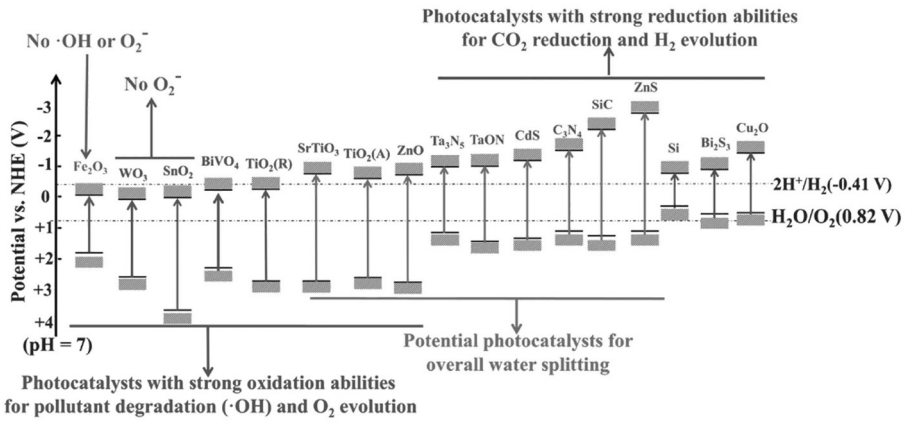

Figure 2. Band positions and potential applications of some typical photocatalysts (at pH = 7 in aqueous solutions). Reprinted from [5].

Apart from the bang gap of the photocatalyst, its structural properties, morphology, adsorption capacity, structure at micro and nanolevel, among others, are also important for the process. For instance, some authors claim that the macro and mesoporosity of the catalyst have influence on the scattering of light, highly porous materials yielding more photo-activated electrons [6, 7].

2.2 g-C_3N_4 as photocatalyst

Recently, g-C_3N_4 has been used as a photocatalyst for a wide range of applications, namely H_2 and O_2 production, CO_2 reduction, nitrogen fixation, pollutant degradation, biocidal treatment, organosynthesis, abatement of nitrogen oxides (NO_x) and metal redox processes [8].

The band positions of g-C_3N_4 are -1.12 and 1.58 eV, allowing a variety of applications (Figure 2). However, the bulk g-C_3N_4 (gCN) material has a small surface area, commonly leading to low photocatalytic efficiencies [8]. Thus, several modification strategies have been pursued to design better g-C_3N_4-based photocatalysts, such as soft templating approaches, exfoliation, elemental doping or heterojunction formation [8]. In this work, a thermal exfoliation treatment was used to increase the surface area of gCN.

Regarding the reactions taking place in the photocatalytic system, Equations 1 to 4 have been proposed for the aforementioned photoactivation of the catalyst, formation of H_2O_2

and ROS [9, 10]. The activation of the catalyst with light (hν), originating the e^-/h^+ pairs, is shown in Equation 1. Electrons will be consumed by oxygen, forming H_2O_2 by the two-electron reduction reaction (Equation 3). Afterwards, H_2O_2 can form $HO^\bullet$ under certain conditions (Equation 4). The competitive $O_2^{\bullet-}$ radicals, which are milder oxidants, are formed by one-electron reduction of oxygen and have to be accounted in the system (Equation 2) [11]. The pollutant can be decomposed by action of the photogenerated holes or by ROS-based oxidation (via attack of $O_2^{\bullet-}$ or $HO^\bullet$).

$$\text{photocatalyst} + h\nu \rightarrow e^- + h^+ \quad (1)$$

$$O_2 + e^- \rightarrow O_2^{\bullet-} \quad (2)$$

$$O_2 + 2\,e^- + 2\,H^+ \rightarrow H_2O_2 \quad (3)$$

$$H_2O_2 + e^- \rightarrow HO^- + HO^\bullet \quad (4)$$

A general literature search of publications dealing with g-C_3N_4-based materials for photocatalytic applications was done by using as keywords “carbon nitride” or “C_3N_4” and “photocatal*” (Figure 3). The application of g-C_3N_4 in photocatalysis is rather recent but gaining an increasing interest, as shown by the evolution of scientific research articles that have been published in the last years. The number of articles increased until 2017 (reaching 834) and 760 articles were published in 2018 until July 6. Considering an exponential growth, more than 1300 publications are predicted for 2018.

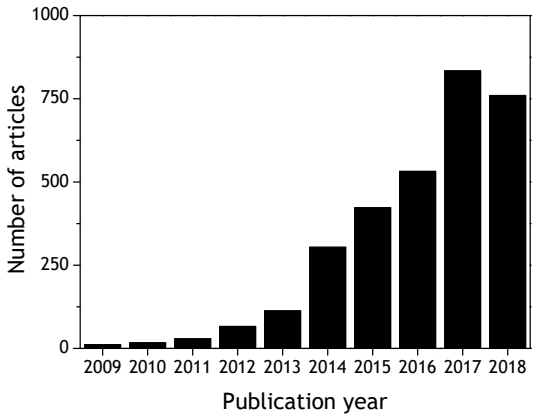

Figure 3. Number of articles published by year. Source: Scopus database, April 26, 2018 (keywords: “carbon nitride” or “C_3N_4” and “photocatal*”).

Considering the large number of publications, another search consisted on “review articles” only, with similar keywords, i.e. “carbon nitride” or “C_3N_4” and “photocatalysis” or “photocatalytic”. The information found within specific review articles is presented in Figure 4, denoting various applications of g-C_3N_4, as well as the

distribution of these studies. Degradation of pollutants and H_2 production are the two major applications of g-C_3N_4 based materials, respectively representing 47% and 34% of the publications. Regarding the degradation of pollutants, more than 80% of the publications consisted in the degradation of dyes (i.e. 38% of all studies found in these review articles), although dyes are not recommended for photocatalytic studies as dyes absorb radiation instead of the catalyst, yielding to possible ambiguous conclusions regarding the true photocatalytic contribution for the degradation of these compounds [12]. The data from this search are summarized in Table A2 for dyes and in Table A1 for other organic compounds (in Appendix A), including the respective methods of synthesis and the removal efficiency in a given reaction time. Surprisingly, in the selected review articles, g-C_3N_4 was always combined with other materials.

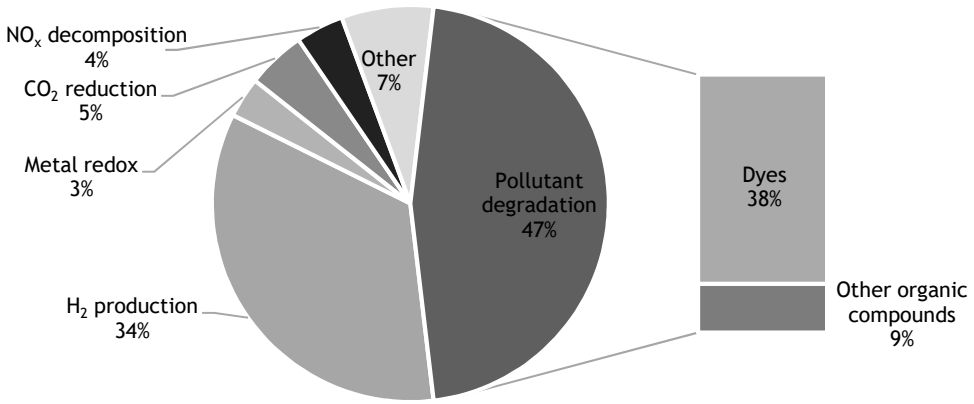

Figure 4. Distribution of g-C_3N_4 applications. Source: Scopus database, January 29, 2018 (keywords: "carbon nitride" or "C_3N_4" and "photocatalysis" or "photocatalytic", and considering studies referred in review articles).

An additional search was performed with more specific terms in order to focus on water or wastewater treatment and metal-free g-C_3N_4 for the degradation of pollutants. The search on Scopus database comprehended the keywords: "carbon nitride" or "C_3N_4" and "photocatalysis" or "photocatalytic" and "pollutant" or "contaminant" or "wastewater treatment" or "water treatment" or "waste water treatment" and "metal free" or "metal-free". Publications dealing with dyes were excluded. Table 1 gathers the information obtained: organic pollutant and its initial concentration, photocatalytic process (some studies referring to photocatalytic ozonation), the catalyst and its preparation method, as well as the removal efficiency. It is interesting to note that all these reports are focused on synthetic water (distilled water as matrix) rather than actual wastewaters. Additionally, in some publications, it was investigated whether the

production and consumption of H_2O_2 occurs (Equations 3 and 4), which will be further discussed on Chapter 2.3.

High removals (> 80%) have been reported for many systems, achieved from 30 to 360 min, with catalyst loads ranging from 0.1 to 1.0 g L^{-1}. The majority of lamps used are Xe lamps (i.e. simulated solar irradiation), with one study reporting natural sunlight and another an energy-saving lamp. Also, it is worth mentioning that from all these publications, three are dealing with photocatalytic ozonation. As expected, photocatalysis in the presence of ozone (i.e., an integration of two oxidation technologies) presents higher pollutant removal efficiencies than those processes applied alone [13], but also a higher cost.

Table 1. Photocatalytic degradation studies using metal-free g-C_3N_4 materials.

Pollutant	Process	Photocatalyst	Operating conditions	Removal efficiency (time)	Ref.
Ammonia	Photocatalysis	Single-layer g-C_3N_4	1.50 mg L^{-1} ammonia; Xe lamp	80% (360 min)	[14]*
Bisphenol A (BPA)	Photocatalysis	O-doped g-C_3N_4	15 mg L^{-1} BPA; 0.02 g catalyst; Xe lamp	100% (180 min)	[15]
Bisphenol A; Oxalic acid (OA)	Photocatalytic ozonation	g-C_3N_4	10 mg L^{-1} BPA; 10 mg L^{-1} OA; 0.5 g catalyst; ozonized O_2 feed; Xe lamp λ > 400 nm	80.0% (120 min)	[16]
4-Chlorophenol (4-CP); Phenol	Photocatalysis	Mesoporous g-C_3N_4	0.12 mmol L^{-1} pollutant; 40 mg catalyst; Xe lamp, λ > 420 nm	100% 4-CP (60 min); 96% phenol (90 min)	[17]*
17-ß-Estradiol (ESD); Ciprofloxacin (CIF)	Photocatalysis	g-C_3N_4, reduced graphene oxide and coal-char composite	20 mg L^{-1} ESD or CIF; 100 mg catalyst; natural sunlight	95.9% ESD (90 min); 92.8% CIF (90 min)	[18]
5-Hydroxymethylfurfural (HMF)	Photocatalysis	g-C_3N_4	0.1 mmol HMF; O_2 feed; Xe lamp	26.7% (360 min)	[19]*
Imidacloprid	Photocatalysis	g-C_3N_4	5 mg L^{-1} imidacloprid; 0.1 g catalyst; energy-saving lamp	90% (300 min)	[20]
Oxalic acid	Photocatalytic ozonation	g-C_3N_4	1 mmol L^{-1} OA; 0.1 g L^{-1} catalyst; Xe lamp; ozonized O_2 feed	100% (30 min)	[21]
Oxalic acid	Photocatalytic ozonation	g-C_3N_4 and reduced graphene oxide	0.11 mmol L^{-1} OA; 0.20 g catalyst; Xe lamp; ozonized O_2 feed	70.6% (40 min)	[22]

Phenol	Photocatalysis	g-C_3N_4	50 mg L^{-1} phenol; 50 mg catalyst; Xe lamp	91% (210 min)	[23]
Sulfachloropyridazine (SCP); Methylene blue (MB)	Photocatalysis	g-C_3N_4 and carbon nanospheres	30 mg L^{-1} SCP and 10 mg L^{-1} MB; 100 mg catalyst	90% SCP (180 min)	[24]
Sulfamethazine (SMZ)	Photocatalysis	g-C_3N_4	5 mg L^{-1} SMZ; 50 mg catalyst; Xe lamp	98% (60 min)	[25]*
5-Sulfosalicylic acid (SSA)	Photocatalysis	g-C_3N_4	10 mg L^{-1} Cr(VI) and 40 mg L^{-1} SSA; 50 mg catalyst; Xe lamp	85% SSA (60 min)	[26, 27]
Tetracycline (TC); Rhodamine B (RhB)	Photocatalysis	g-C_3N_4 and hexagonal boron nitride	10 mg L^{-1} TC and 20 mg L^{-1} RhB; 100 mg catalyst; Xe lamp, $\lambda > 420$ nm	79.7% TC (60 min); 99.5% RhB (40 min)	[28]*

*Reports where H_2O_2 formation was observed.

2.3 Production of H_2O_2 using g-C_3N_4

As mentioned previously, the degradation of pollutants can be enhanced in the presence of H_2O_2 because it can be decomposed to ROS. Therefore, H_2O_2 production is an important advantage of using g-C_3N_4 as photocatalyst for the degradation of organic pollutants. The production of H_2O_2 occurs via the molecular oxygen reduction reaction (ORR) by the photogenerated electrons on the semiconductor conduction band and with protons from the dissolved compounds.

H_2O_2 generation depends on the catalyst surface properties. Several photocatalysts may be considered for the production of H_2O_2, but their band gap may enable one-electron or four-electron O_2 reduction, respectively leading to $O_2^{\bullet-}$ or water formation, and decreasing the selectivity towards H_2O_2 generation [29, 30]. As reported, O_2 on gCN preferably undergoes reduction to $O_2^{\bullet-}$ via one-electron reduction [31], while on modified g-C_3N_4 materials, with more surface defects, O_2 preferably suffers two-electron reduction to form H_2O_2.

In this way, the generation of H_2O_2 can be achieved in the presence of a specific catalyst, such as exfoliated g-C_3N_4, a proton donor (e.g., an organic pollutant) and oxygen, namely following Equation 3. In the particular case of g-C_3N_4, as shown in Figure 5, photoactivated electrons react with O_2 and cause the formation of superoxide radicals when using an alcohol as sacrificial agent, the presence of 1,4-endoperoxide species resulting in the formation of H_2O_2. At the same time, the sacrificial agent, as an alcohol or even water, undergo oxidation and yield protons that aid the formation of H_2O_2.

In some of the publications listed in Table 2, the formation of H_2O_2 was observed in the presence of both visible light and a g-C_3N_4 catalyst [14, 17, 19, 25, 28]. For instance, the addition of benzoquinone and isopropanol proved that $O_2^{\bullet-}$ and $HO^{\bullet}$ radicals are the main oxidizing species, and the addition of ethylenediamine tetraacetic acid (EDTA) proved that photoactivated holes have less influence on the degradation of the pollutants [23]. It was also proved that higher concentrations of H_2O_2 were obtained with a mesoporous g-C_3N_4 material than with gCN [17]; however, an excessive amount of H_2O_2 could decrease the photon adsorption on the catalyst [25].

Figure 5 shows the photoactivation of g-C_3N_4 with the C1 and N4 atoms negatively charged, attracting oxygen that will later react with the trapped protons in nearby N atoms. The sacrificial agent shown in Figure 5 is a generic alcohol that yields an aldehyde.

Ethanol, propan-2-ol, butan-2-ol and benzyl alcohol are examples of alcohols that have been studied with a g-C_3N_4 catalyst being observed the H_2O_2 production [32]. For instance, ethanol yields acetaldehyde and H_2O_2 (with a very high selectivity to H_2O_2 - 90%).

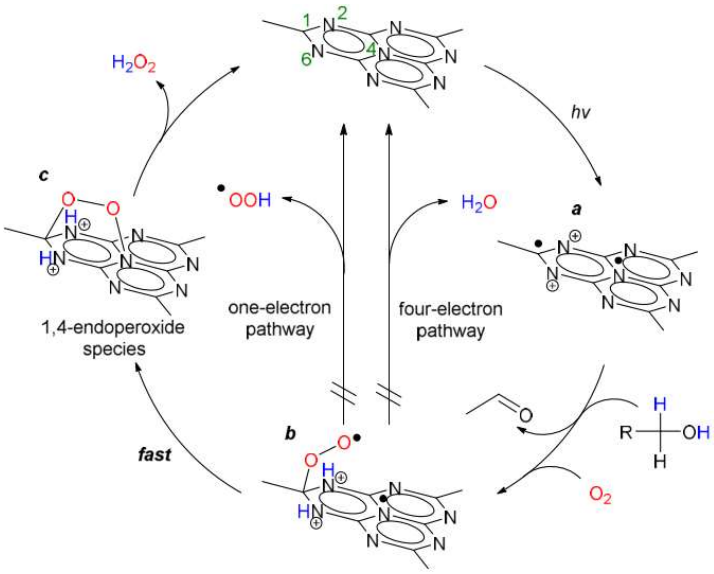

Figure 5. Proposed mechanism for selective formation of H_2O_2 on the photoactivated g-C_3N_4 surface. Reprinted from [30].

The generation or even addition of H_2O_2 promotes the degradation of the pollutants as it causes the production of $HO^{\bullet}$ in the presence of light, depending on the radiation emitting wavelength and catalyst employed [17, 18, 25, 33]. The use of catalysts with more -OH groups, such as TiO_2, also can lead to greater formation of $HO^{\bullet}$ radicals [34]. The addition of ozone similarly promotes the photodegradation (i.e. photocatalytic ozonation) due to enhanced formation of ROS of direct ozone attack to the pollutant molecules, in one study yielding a greater degradation efficiency than the H_2O_2-assisted photocatalytic experiments [18].

Adding more surface defects to the catalyst can lead to a faster and more productive formation of H_2O_2 [30]. The doping of g-C_3N_4 may also be beneficial, such as the catalyst used by Kofuji et al. [29] which hinders the recombination of the electron-hole pairs, allowing for a more efficient production of H_2O_2.

Shiraishi et al. [35] stated that the photocatalytic activity for H_2O_2 formation increases with the addition of pyromellitic diimide units on g-C_3N_4, as this modification causes a shift of the catalyst's valence band. In that work, up to 50.6 μmol of H_2O_2 were produced in 48 h. Kofuji et al. [29] mentioned that the addition of biphenyl diimide also leads to H_2O_2 formation (up to 11.6 μmol in 24 h), but with a suppressed rapid recombination of electron-hole pairs that promotes the catalytic activity. Kofuji et at. [36] prepared

mellitic triimide-doped g-C_3N_4 for photocatalytic H_2O_2 production, reaching an amount of 27.5 μmol of H_2O_2 in 24 h. Zhao et al. [37] combined carbon nanotubes with g-C_3N_4, with 48.7 μmol of H_2O_2 being achieved at 60 min.

The highest values for H_2O_2 generation in each study are shown in Table 2. Additionally, the experimental conditions used during the photocatalytic experiments and the modification performed over g-C_3N_4 are also presented. The H_2O_2 production is shown in terms of: highest amount of H_2O_2 produced (μmol); moles of H_2O_2 per catalyst load; and moles of H_2O_2 per catalyst load and time.

Table 2. Metal-free g-C_3N_4 photocatalytic studies reporting H_2O_2 production.

Modification on g-C_3N_4	H_2O_2 production	Experimental conditions	Ref.
Pyromellitic diimide doping	39 μmol (48 h) 788 μmol g_{cat}^{-1} 16 μmol g_{cat}^{-1} h^{-1}	27 mL propan-2-ol; 3 mL water; 50 mg catalyst; O_2 saturation; Xe lamp $\lambda \geq 420$ nm	[35]
Pyromellitic diimide doping	210 μmol (6 h) 4200 μmol g_{cat}^{-1} 700 μmol g_{cat}^{-1} h^{-1}	30 mL water; 50 mg catalyst; O_2 saturation; Xe lamp $\lambda \geq 420$ nm	[35]
None	30 μmol (12 h) 1500 μmol g_{cat}^{-1} 125 μmol g_{cat}^{-1} h^{-1}	4.5 mL ethanol; 0.5 mL water; 20 mg catalyst; O_2 saturation; Xe lamp $\lambda \geq 420$ nm	[32]
None	109 μmol (12 h) 5450 μmol g_{cat}^{-1} 454 μmol g_{cat}^{-1} h^{-1}	4.5 mL benzyl alcohol; 0.5 mL water; 20 mg catalyst; O_2 saturation; Xe lamp $\lambda \geq 420$ nm	[32]
SiO_2 templating	90 μmol (24 h) 4500 μmol g_{cat}^{-1} 188 μmol g_{cat}^{-1} h^{-1}	4.5 mL ethanol; 0.5 mL water; 20 mg catalyst; O_2 saturation; Xe lamp $\lambda \geq 420$ nm	[30]
Biphenyl diimide doping	12 μmol (24 h) 232 μmol g_{cat}^{-1} 10 μmol g_{cat}^{-1} h^{-1}	30 mL water; 50 mg catalyst; O_2 saturation; solar simulator λ = 420-500 nm	[29]
Biphenyl diimide doping	40 μmol (48 h) 400 μmol g_{cat}^{-1} 8 μmol g_{cat}^{-1} h^{-1}	30 mL water; 100 mg catalyst; O_2 saturation; solar simulator λ = 420-500 nm	[29]
Mellitic triimide doping	28 μmol (24 h) 550 μmol g_{cat}^{-1} 23 μmol g_{cat}^{-1} h^{-1}	30 mL water; 50 mg catalyst; O_2 saturation; Xe lamp $\lambda \geq 420$ nm	[36]

Carbon vacancies	≈90 μmol (60 min) ≈900 μmol g_{cat}^{-1} ≈900 μmol g_{cat}^{-1} h^{-1}	100 mL water; 100 mg catalyst; Xe lamp $\lambda \geq 420$ nm	[38]
Perylene imide heterojunction	120 μmol (120 min) 2400 μmol g_{cat}^{-1} 1200 μmol g_{cat}^{-1} h^{-1}	50 mL water; 50 mg catalyst; Xe lamp $\lambda \geq 420$ nm	[39]
Thermal exfoliation	83 μmol (30 min) 1650 μmol g_{cat}^{-1} 3300 μmol g_{cat}^{-1} h^{-1}	50 mL water; 20 mg L^{-1} phenol; 1 g L^{-1} catalyst; LEDs λ = 416 nm	[40]
Carbon nanotubes coupling	130 μmol (24 h) 1302 μmol g_{cat}^{-1} 54 μmol g_{cat}^{-1} h^{-1}	5 mL formic acid; 95 mL water; 0.1 g L^{-1} catalyst; O_2 saturation; Xe lamp $\lambda \geq 400$ nm	[37]
Thermal exfoliation	59 μmol (30 min) 2370 μmol g_{cat}^{-1} 4741 μmol g_{cat}^{-1} h^{-1}	50 mL water; 60 mg L^{-1} phenol; 0.5 g L^{-1} catalyst; O_2 saturation; LEDs λ = 417 nm	This study
Thermal exfoliation	40 μmol (15 min) 1613 μmol g_{cat}^{-1} 6452 μmol g_{cat}^{-1} h^{-1}	50 mL water; 108.5 mg L^{-1} gallic acid; 0.5 g L^{-1} catalyst; O_2 saturation; LEDs λ = 417 nm	This study
Thermal exfoliation	114 μmol (60 min) 4470 μmol g_{cat}^{-1} 4570 μmol g_{cat}^{-1} h^{-1}	50 mL water; 70.2 mg L^{-1} resorcinol; 0.5 g L^{-1} catalyst; O_2 saturation; LEDs λ = 417 nm	This study

3 Materials and methods

3.1 Reagents

Dicyandiamide ($C_2H_4N_4$, 99%), phenol (C_6H_5OH, 99%), titanium(IV) oxysulfate (TiO_5S, ~15 wt. % in dilute sulfuric acid), hydrogen peroxide (H_2O_2, 30 wt. % in water), hydroquinone ($C_6H_6O_2$, 99%), hydrochloric acid (HCl, 37%), sodium hydroxide (NaOH, 97.0%), acetic acid (CH_3CO_2H, 99.7%), tyrosol ($C_8H_{10}O_2$, 98%) and caffeine ($C_8H_{10}N_4O_2$, 98%) were obtained from Sigma-Aldrich. Sodium chloride (NaCl, 99.5%) was obtained from Merck Millipore. Methanol (CH_3OH, ≥99.8%) and acetonitrile (CH_3CN, 99.9%) were obtained from VWR. Sodium sulfite anhydrous (Na_2SO_3, 98%), sulfuric acid (H_2SO_4, 99%), benzoquinone ($C_6H_4O_2$, 99%), catechol ($C_6H_6O_2$, 98%), resorcinol ($C_6H_6O_2$, 98%), benzoic acid ($C_6H_5CO_2H$, 99%), 4-hydroxybenzoic acid ($C_7H_6O_3$, 99%), protocatechuic acid ($C_7H_6O_4$, 97%), gallic acid ($C_7H_6O_5$, 98%) and 4-methoxyphenol ($C_7H_8O_2$, 98%) were obtained from Honeywell Fluka. Ultrapure water was produced in a Direct-Q Millipore system (Merck Millipore, Billerica, MA, USA).

3.2 Catalyst preparation

The synthesis of gCN was performed by thermal decomposition of dicyandiamide [41], forming melamine, melem, melon and lastly g-C_3N_4 (Figure B1, Appendix B). The polymeric structure of g-C_3N_4 is composed of aggregates of deaminated melem units.

The precursor was placed in a semi-closed crucible in a muffle furnace under static air atmosphere. The equipment was programed to heat at 2 °C min^{-1} until 450 °C with this temperature being maintained during 2 h, followed again by a ramp heating until 550 °C and maintained at this temperature for 4 h. Afterwards, the material was powdered in a mortar, rinsed with ultra-pure water, filtered and dried overnight in a drying oven.

As described by Lima et al. [41], gCN suffered a thermal post-treatment producing an exfoliated material designated as gCN_T. This catalyst was prepared by spreading 1.2 g of gCN in an open crucible inside a muffle furnace programmed to heat at 2 °C min^{-1} until 500 °C, this temperature being maintained for 2 h.

3.3 Catalyst characterization

3.3.1 Scanning electron microscopy

The morphology of the catalyst was analyzed by scanning electron microscopy (SEM) using a FEI Quanta 400FEG ESEM/EDAX Genesis X4 M instrument.

3.3.2 Diffuse reflectance ultraviolet-visible spectroscopy

The catalyst was characterized by diffuse reflectance ultraviolet-visible spectroscopy (DRUV-Vis) in a Jasco V-560 spectrometer equipped with an integrating sphere attachment (Jasco ISV-469). The retrieved spectra were recorded in diffuse reflectance mode and converted to equivalent absorption Kubelka–Munk (KM) units.

3.3.3 Point of zero charge

Six solutions of 50 mL of NaCl 0.01 M were prepared with pH ranging from 2 to 12, by adjusting with HCl solutions of 0.1 M and 0.01 M, and NaOH 0.1 M and 0.01 M. 150 mg of gCN_T were then added to each solution and left in the dark for 24 h under continuous stirring. The pH in the point of zero charge (PZC) was obtained from the interception of the final pH vs. initial plot with the final pH = initial pH plot.

3.3.4 Zeta potential

The zeta potential of gCN and gCN_T particles was determined by dynamic light scattering using a Malvern Zetasizer Nano ZS equipment (Malvern Instruments Ltd, UK). For this end, solutions with 2 mg of material were dispersed in 10 mL of distilled water by sonication at room temperature.

3.4 Ultraviolet-visible spectroscopy

The ultraviolet-visible (UV-vis) spectrum of each compound (200 – 800 nm) was obtained by analyzing samples diluted in ultrapure water (Figure C2, Appendix C). Then, the maximum absorption wavelength (λ_{max}) of each compound was determined (Table C1) and selected for high performance liquid chromatography (HPLC) analysis using a diode array detector (section 3.6.1).

3.5 Photocatalytic experiments

A glass reactor with a maximum capacity of 100 mL was employed in photocatalytic experiments. The experiments were performed under visible light irradiation using 10 W LEDs with an emission line peaking at 417 nm (Figure C1, Appendix C), located

symmetrically from the outside at 4.0 cm from the reactor wall. The average irradiance of each LED reaching the reactor wall was 112.6 mW cm^{-2}.

In a typical experiment, 50 mL of an aqueous suspension containing the pollutant and the catalyst powder was sonicated in an ultrasound bath and stirred in the dark for 30 min to reach the adsorption-desorption equilibrium. Air was continuously bubbled during the photocatalytic reaction (except when referred other situation) and the suspension was magnetically stirred.

The initial concentration of each pollutant was kept at 0.64 mmol L^{-1} (equivalent to 60 mg L^{-1} of phenol) and the catalyst load varied from 0.1 to 1.0 g L^{-1}. After centrifugation and filtration, the collected samples were analyzed by HPLC and UV-vis spectrophotometry for determining the concentration of pollutant and H_2O_2, respectively. For total organic carbon (TOC) determination, the samples were withdrawn from the reactor, centrifuged, filtered and mixed with an excess of sodium sulfite (± 2 mg) in order to decompose H_2O_2.

For studying the effect of the O_2 partial pressure (resulting in different concentrations of oxygen dissolved in the liquid phase), different mixtures of O_2 and Ar were used, whose composition were controlled by using Bronkhorst High-Tech EF-FLOW Select F-201 CV thermal mass flow meters.

3.6 Analytical methods

3.6.1 High performance liquid chromatography

Samples periodically withdrawn during the photocatalytic reactions were analyzed by high performance liquid chromatography (HPLC) using a Hitachi Elite LaChrom instrument (Hitachi, Ibaraki, Japan) equipped with a diode array detector (L-2450), a Purospher Star RP-18 column (250 mm × 4.6 mm, 5 mm particles), and a solvent delivery pump (L-2130) at a fixed flow rate of 1 mL min^{-1}.

In the case of phenol, catechol, resorcinol, hydroquinone, benzoquinone and caffeine, the HPLC method starts with an equilibrated mixture of water (A):methanol (B) (70:30) followed by a linear gradient step to A:B (37:63) in 20 min. Finally, the initial conditions were reestablished in a 1 min gradient step and the A:B (70:30) mixture was isocratically eluted for 7 min.

For benzoic acid, 4-hydroxybenzoic acid, protocatechuic acid, gallic acid, 4-methoxyphenol and tyrosol, the concentration of the individual compounds was followed using an optimized gradient elution method at a flow rate of 1 mL min^{-1} and the

respective λ_{max} (Appendix C). Firstly, the column was equilibrated with an A:B (10:90) mixture of 1% acetic acid and 0.5% acetonitrile in methanol (A) and 1% acetic acid in water (B). Then, the following program was used: isocratic elution for 15 min followed by a linear gradient run to A:B (60:40) in 27 min and finally to A:B (10:90) in 5 min.

3.6.2 H_2O_2 concentration

For the determination of the amount of H_2O_2 produced during the photocatalytic reactions, a mixture of 300 µL of the sample, 300 µL of sulfuric acid (0.5 M) and 10 µL of titanium oxysulphate were mixed in a quartz cuvette and the absorbance read at a wavelength of 405 nm by an OceanOptics USB2000 + UV–vis spectrometer.

3.6.3 TOC content

The TOC content was determined using a Shimadzu TOC-5000A apparatus. TOC removal is an important parameter in water and wastewater treatment since TOC accounts for the parent pollutant and its oxidation products. The initial theoretical TOC content was calculated for a phenol solution, by using Equation 5.

$$TOC_{theoretical} = \frac{\begin{pmatrix}\text{mass concentration of}\\ \text{compound in the solution}\end{pmatrix}}{(\text{molar mass of compound})} \cdot \begin{pmatrix}\text{molar mass of}\\ \text{carbon in the compound}\end{pmatrix} \quad (5)$$

For instance, for an initial phenol concentration of 60 mg L^{-1}, the theoretical TOC value is 46 mg L^{-1} and the experimental one was 47 mg L^{-1}. To understand the possible impact of some catalyst passing the filter before TOC measurements, experiments using only ultrapure water (UP H_2O), and ultrapure water with catalyst and with and without adding sodium sulfite, were performed measuring the TOC content at the end of 180 min (Table 3). The TOC value obtained for UP H_2O can be considered negligible, while the value obtained when gCN_T is present in water may be attributed to the presence of very small gCN_T particles that were not retained in the filter passing to the aqueous phase. As expected, the addition of sodium sulfite did not produce any significant change in the TOC value.

Table 3. TOC values obtained for different systems.

Reactive medium	TOC at 180 min (mg L^{-1})
UP H_2O	0.29
UP H_2O + gCN_T	1.87
UP H_2O + gCN_T + sodium sulfite	2.13

3.6.4 pH

The pH of solutions was measured using a 211 Microprocessor pH meter by HANNA Instruments.

3.6.5 Dissolved oxygen and temperature

Dissolved oxygen (DO) and the temperature (*T*) of the solution were determined using a Crison Oxi 45 portable oximeter.

3.7 Degradation kinetic studies

In the presence of photoactivated gCN_T, it is known that phenol decomposes yielding catechol, hydroquinone and benzoquinone, which are further oxidized forming aliphatic acids, carbon dioxide and water as the final degradation products [40, 42].

Moreover, the reaction rate for photocatalytic reactions commonly follows a pseudo-first order based on the Langmuir-Hinshelwood mechanism [43, 44]. Considering that oxygen is saturated in the liquid phase, the degradation reaction is described by Equation 6 relating the rate of degradation, *r*, with the rate constant, *k*, and the concentration of the compound, *C*.

$$r = k\,C \tag{6}$$

A simple integration of Equation 6 and its rearrangement in terms of the normalized concentration of the pollutant (C/C_0) results in Equation 7. Thus, curve fitting of this equation was applied to the data points represented in terms of C/C_0 as function of *t*.

$$\frac{C}{C_0} = e^{-k\,t} \tag{7}$$

4 Results and discussion

4.1 Catalyst characterization

The thermally exfoliated g-C_3N_4 (gCN_T) material used in this dissertation was extensively characterized by Lima et al. [41], who reported the enhanced photocatalytic activity of this material for the conversion of benzyl alcohol into benzaldehyde. Some additional characterization results are included in the present dissertation.

4.1.1 SEM analysis

The morphology of gCN and gCN_T at microlevel was observed by SEM. In Figure 6, it is clearly shown that bulk g-C_3N_4 is composed by compact aggregates, whereas exfoliated g-C_3N_4 (i.e., gCN_T) consists of thin layers of carbon nitride. This is due to the breaking of bonds which do not withstand the high temperatures of the thermal treatment of gCN. The bonds between g-C_3N_4 layers (van der Waals forces) are oxidized, occurring the splitting of these layers. Accordingly, an increase in the BET surface area, from 4 m^2 g^{-1} of gCN to 87 m^2 g^{-1} of gCN_T, was observed by Lima et al. [41].

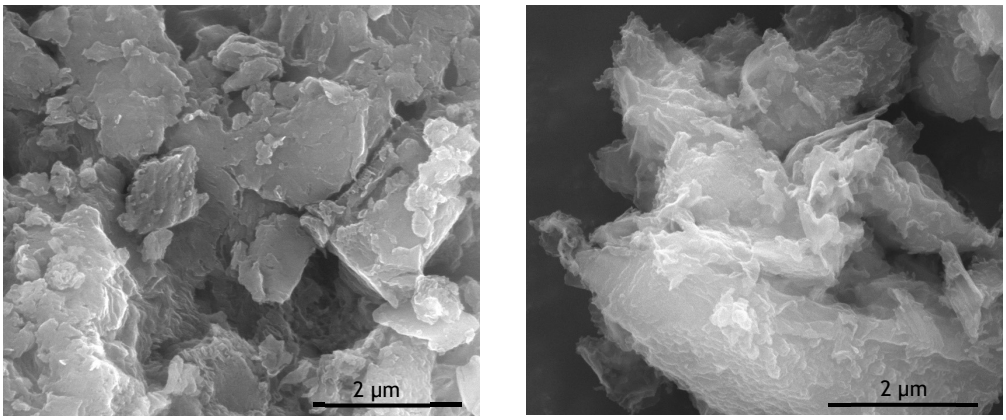

Figure 6. SEM micrographs of bulk (left) and exfoliated (right) g-C_3N_4.

4.1.2 DRUV-Vis

The DRUV-vis spectrum and the Tauc plot of gCN_T were determined (Figure 7). gCN_T shows an intense absorption band with absorption edge at 480 nm. The band gap, determined from the respective Tauc plot, is 2.73 eV.

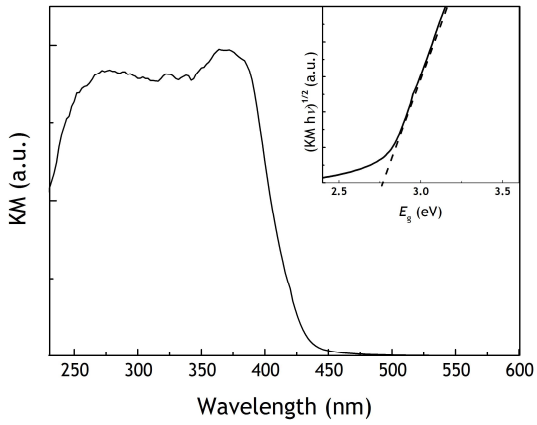

Figure 7. DRUV-Vis spectrum and Tauc plot (inset) of gCN_T.

4.1.3 Point of zero charge

The point of zero charge (PZC) of a material characterizes its surface chemistry, which can be one of the indicators of its performance. As described before (section 3.3.3), gCN_T was dispersed in aqueous acidic and alkaline solutions. The catalyst's acidic groups tend to lose protons to the solution leaving the surface negatively charged, while alkaline groups tend to attract protons from the solution and the surface becomes positively charged. For a certain value of pH, the total surface charge will be zero, which corresponds to the pH_{PZC} [45].

In the structure of g-C_3N_4 (Figure B1, Appendix B) there are primary, secondary and tertiary amine groups. Primary and secondary amines can accept both HO^- and H^+ from the solution, and tertiary amine groups can only accept H^+ [46]. Equations 8-11 display the changes in carbon nitride surface charges based on the equilibrium between the secondary and primary amino groups from the melem units with the reactive medium [47].

Figure 8 indicates that gCN_T had a pH_{PZC} value of 6.3. Moreover, gCN_T seems to have amphoteric properties. In this way, the material surface is negatively charged for pH values greater than 6.3, whereas the surface is positively charged for values lower than 6.3. Different values were found in the literature for the pH_{PZC} of g-C_3N_4, ranging from 4.1 to 5.1 and depending on the precursor used in the preparation of this material [47, 48]. For cyanamide, thiourea, melamine and urea, the reported pH_{PZC} values were 4.1, 4.4, 5.0 and 5.1, respectively.

$$\equiv C{-}NH_2 + H^+ \rightarrow \equiv C{-}NH_3^+ \quad (8)$$

$$\equiv C{-}NH_2 + HO^- \rightarrow \equiv C{-}NH^- + H_2O \quad (9)$$

$$(\equiv C)_2{-}NH + H^+ \rightarrow (\equiv C)_2{-}NH_2^+ \quad (10)$$

$$(\equiv C)_2{-}NH + HO^- \rightarrow (\equiv C)_2{-}N^- + H_2O \quad (11)$$

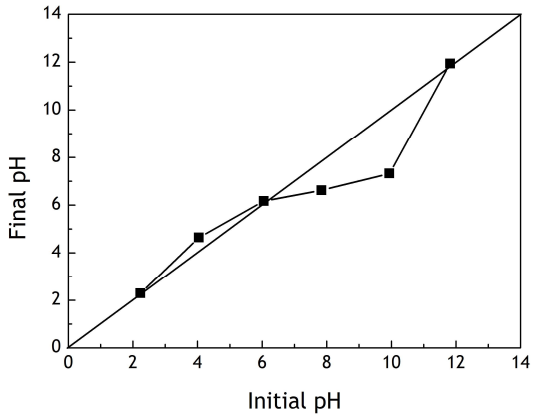

Figure 8. Point of zero charge of gCN_T.

4.1.4 Zeta potential

Zeta potential measurements revealed that gCN_T was slightly more stable than gCN dispersed in water, i.e. the zeta potential of gCN_T is more negative than that of gCN (-30.4 and -29.3 mV, respectively).

4.1.5 Band gap energy

The band gap energies of gCN and gCN_T, determined from the respective Tauc plots, are 2.68 and 2.73 eV, respectively. The valence and conduction band levels were calculated by Equations 12 and 13 [40] and the values obtained were 1.51 and -1.22, respectively.

$$E_{VB} = X - E^0 + 0.5\, E_g \quad (12)$$

$$E_{CB} = E_{VB} - E_g \quad (13)$$

E_{VB} is the valence band edge potential, E_{CB} is the conduction band edge potential, X is the electronegativity of a semiconductor obtained as a geometric mean of the constituent atoms (4.5 eV for g-C_3N_4 [49]), E^0 is energy of free electrons *vs* vacuum (4.5 eV) and E_g is the absorption edge potential (experimentally determined).

According to the calculated band levels, a preliminary study of the redox reactions can be performed. Equations 2-4 show similar redox potentials which enables their possible competitive occurrence on the catalyst conduction band. The formation of $O_2^{\bullet-}$ or H_2O_2 show potentials of -0.35 V [50] and +0.68 V [40, 51], respectively. The degradation of H_2O_2 to form $HO^\bullet$ radicals has a potential of +0.39 V [50]. Additionally, the reduction of $HO^\bullet$ to water is +2.31 V [50] and the direct oxidation of phenol with photoactivated h^+ has a potential of +1.76 V [52]. Since the CB energy level of gCN_T is -1.22 eV, $O_2^{\bullet-}$ generation possibly happens preferably than H_2O_2 production. In this way, according to their redox potentials, the expected

reactions on the CB are Equations 2, 4 and 3. On the VB, direct oxidation of phenol occurs preferentially to water autoxidation (with a potential of +1.23 V).

4.2 Case study of phenol

Phenol was the model compound in the performed experiments. An initial concentration of 60 mg L^{-1} was used since a good compromise between phenol degradation and H_2O_2 production in the presence of visible light and g-C_3N_4 was found in preliminary studies for this concentration of phenol [53]. The results of the experiments performed using phenol, namely the kinetic studies, the influence of catalyst load and oxygen in the degradation of phenol, and the H_2O_2 production and TOC removal, are shown in this section.

4.2.1 Catalyst load

The photocatalytic degradation of phenol (Figure 9 - left) and the possible H_2O_2 production (Figure 9 - right) were studied for different catalyst loads, ranging from 0.10 to 1.50 g L^{-1}, while all the other experimental conditions were maintained the same. The photolysis of phenol is shown in Figure 9, which is negligible. Moreover, H_2O_2 was not detected in this experiment. These results were expected since phenol only absorbs light at wavelengths below 300 nm and the LEDs emitted at 417 nm (Figure C1, Appendix C). Thus, the catalyst can be photoexcited by these LEDs, but degradation of phenol is not possible in the absence of the photocatalyst. For catalyst loads between 0.50 and 1.50 g L^{-1}, phenol removal efficiencies higher than 90% are obtained at 60 min, and the highest concentration of H_2O_2 was registered for 0.50 g L^{-1} of catalyst. It is worth mentioning that the H_2O_2 concentration increases and then decreases with an exception for the lowest catalyst load (0.10 g L^{-1}), the maximum H_2O_2 concentration (Figure 9 - right) normally being reached when phenol is nearly completely degraded (Figure 9 - left), i.e. at 60 min.

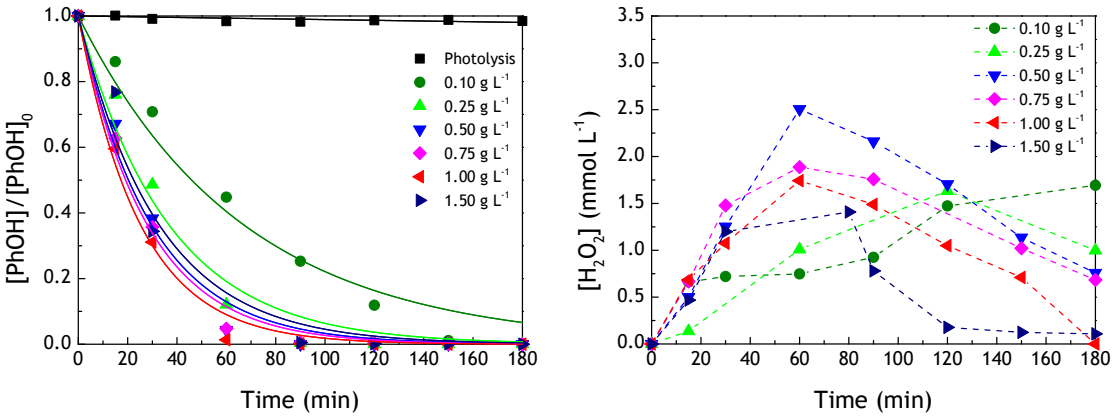

Figure 9. Phenol normalized concentration ([PhOH]/[PhOH]$_0$) (left) and H_2O_2 production (right) for different gCN_T catalyst loads.

For easier interpretation, the results are summarized in Figure 10, where both phenol removal and H_2O_2 concentration values correspond to 60 min of reaction. Therefore, it is concluded the best compromise between the degradation of phenol and production of H_2O_2 was really achieved using 0.5 g L^{-1} of gCN_T.

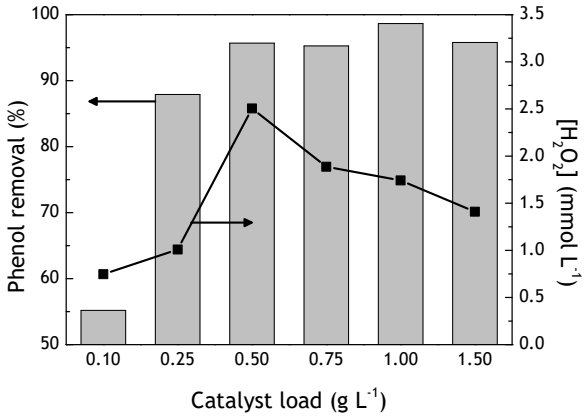

Figure 10. Phenol removal efficiency and H_2O_2 concentration at 60 min of reaction for different catalyst loads.

Fitting the model of Equation 7 to the experimental data (Figure 9 - left), the pseudo first-order reaction rate constants (k_{app}) for phenol degradation were obtained and shown in Figure 11, as a function of catalyst load. k_{app} increases markedly up to 0.50 g L^{-1} of catalyst load (k_{app} = 0.033 min^{-1}), the highest value (k_{app} = 0.040 min^{-1}) being achieved for a catalyst load of 1.00 g L^{-1}.

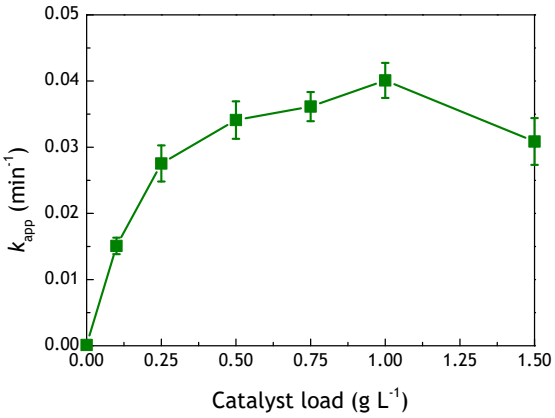

Figure 11. Apparent first-order reaction rate constant (k_{app}) for phenol degradation (C_0 = 60 mg L^{-1}) and different gCN_T catalyst loads.

The TOC content was also determined, a remarkable TOC removal being achieved for catalyst loads higher than 0.5 g L^{-1} (Figure 12).

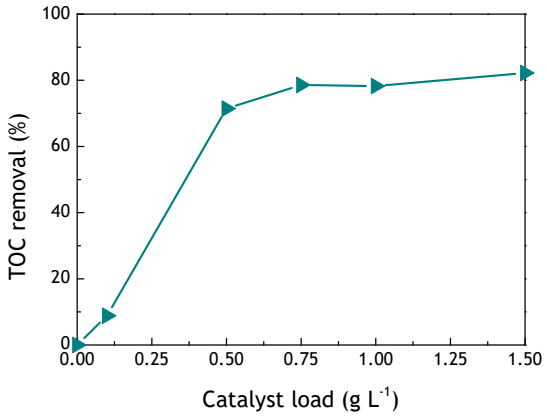

Figure 12. TOC removal obtained for different gCN_T catalyst loads.

4.2.2 Degradation and mineralization of phenol (catalyst load of 0.5 g L^{-1})

Experiments were then conducted with a catalyst load of 0.5 g L^{-1}, considering that the highest H_2O_2 concentration was achieved with this catalyst load (Figure 10) as well as high phenol and TOC removals. Many replicate experiments were done with this catalyst load to determine the data deviations (Figure 13) and the TOC removal as a function of time (Figure 14), and to better understand the system under study. As observed before, a peak of maximum H_2O_2 concentration is obtained at 60 min of reaction when most of phenol was removed (Figure 13). After that time, the H_2O_2 concentration decreases since phenol was completely removed from the solution.

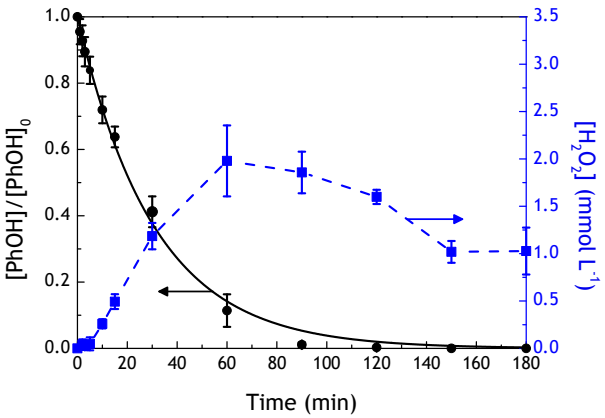

Figure 13. Phenol normalized concentration ($[PhOH]/[PhOH]_0$) and H_2O_2 production by photocatalysis (0.50 g L^{-1} catalyst load) - replicates.

The TOC content was then determined at different reaction times (Figure 14), each data point (or two of them) corresponding to a single experiment in order to have enough volume of sample for TOC analysis. After 180 min, the TOC content is 11.2 mg L^{-1}, corresponding to 77.2% of phenol mineralization. Thus, reaction by-products such as low molecular weight carboxylic

acids were formed, since phenol was removed to levels below the limit of quantification (Figure 13) and catechol, benzoquinone or hydroquinone (known aromatic intermediates formed during phenol degradation) were not detected. The TOC removal increased to 87.2% in 360 min of irradiation (TOC content in the liquid phase of 7.8 mg L^{-1}), but it is important to notice that for such low TOC values, there is an interference resulting from some suspended gCN_T and from the sodium sulfite that was added to decompose H_2O_2 before analysis (Table 3).

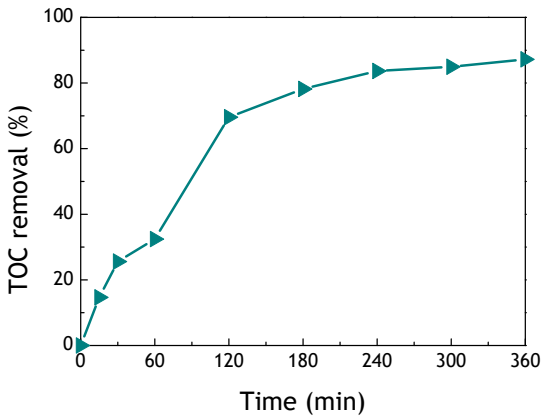

Figure 14. TOC removal evolution in the photocatalytic degradation of phenol (0.50 g L^{-1} catalyst load).

Formic, fumaric, maleic, malonic, muconic, oxalic and pyruvic acids, are some of the known phenol aliphatic oxidation by-products [40]. In the present dissertation, malic, malonic, fumaric and formic acids were detected, but not quantified due to their very low concentrations. Moreover, the pH was measured in one of the photocatalytic experiments (Figure 15), the initial pH ≈ 6 decreasing to a pH ≈ 4 in 30 min.

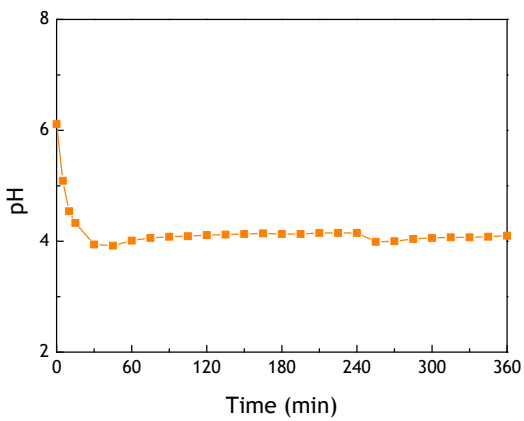

Figure 15. pH evolution in the photocatalytic degradation of phenol (0.50 g L^{-1} catalyst load).

The same experiment was repeated but analyzing the TOC removal during the adsorption-desorption equilibrium studied in dark conditions, turning-on the LEDs at 0 min and turning-off these LEDs after 30 min (Figure 16), the TOC content remaining constant in the absence of light.

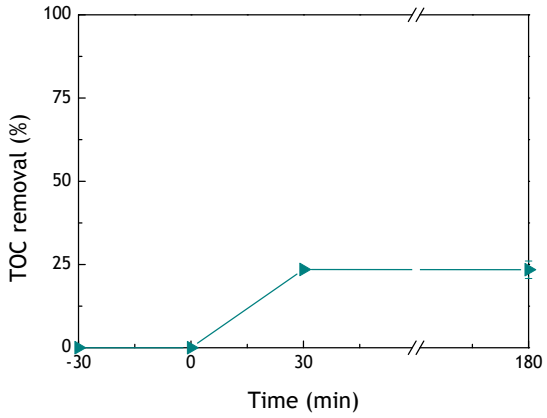

Figure 16. TOC removal evolution in the photocatalytic degradation of phenol, turning-off the LEDs after 30 min (0.50 g L^{-1} catalyst load).

4.2.3 H_2O_2 production

As mentioned in Chapter 2.3, H_2O_2 is expected to be produced in the presence of the studied photoactivated material, a proton donor and molecular oxygen. The H_2O_2 formation and decomposition were studied separately to better understand this system and the results are shown in the present section, together with those obtained by changing target parameters.

4.2.3.1 Formation of H_2O_2

Experiments were performed with focus on four parameters, namely in the absence of: oxygen (O_2), by using argon (Ar); the proton donor, in this case, phenol (PhOH); photocatalyst (gCN_T), corresponding to photolysis; and light (h*v*); i.e. experiments # 2, 3, 4, and 5 in Table 4, respectively. It can be concluded that H_2O_2 is produced only in the presence of all the four parameters (experiment #1).

Table 4. Experiments performed to study the H_2O_2 production.

Experiment	h*v*	gCN_T	PhOH	O_2	**H_2O_2 production**
1	✕	✕	✕	✕	Yes
2	✕	✕	✕		No
3	✕	✕		✕	No
4	✕		✕	✕	No
5		✕	✕	✕	No

4.2.3.2 Decomposition of H_2O_2

In this set of experiments, H_2O_2 was added at the beginning of the run (ca. 1 - 3 mmol L^{-1}), and six experimental conditions were studied, as summarized in Table 5. The H_2O_2 decomposition is inhibited only in the absence of the photocatalyst (experiment #7) or light (experiment #8), thus both are responsible for a notorious H_2O_2 decomposition.

Table 5. Experiments performed to study the H_2O_2 decomposition.

Experiment	H_2O_2	hν	gCN_T	PhOH	O_2	**H_2O_2 decomposition**
6	✕	✕	✕	✕	✕	Yes
7	✕	✕			✕	No
8	✕		✕	✕	✕	No
9	✕	✕	✕		✕	Yes
10	✕	✕	✕			Yes
11	✕	✕	✕	✕		Yes

In addition, Figure 17 demonstrates that in the experiment #6 (H_2O_2 + hν + gCN_T + PhOH + O_2), H_2O_2 is formed until nearly all phenol was degraded (60 min), then being decomposed.

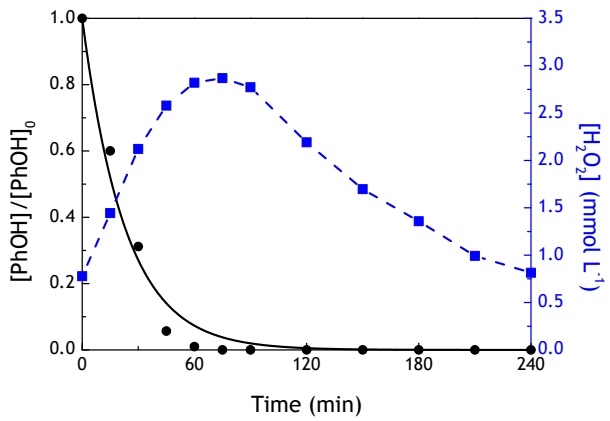

Figure 17. Phenol degradation and H_2O_2 production for a photocatalytic experiment with addition of H_2O_2 at t = 0 min (experiment #6 in Table 5: H_2O_2 + hν + gCN_T + PhOH + O_2).

Under dark conditions (experiment #8), the concentrations of both phenol and H_2O_2 remained the same (results not shown), demonstrating that phenol is not removed by adsorption on the catalyst surface. In the absence of phenol with (experiment #9) or without (experiment #10) oxygen, H_2O_2 was fully decomposed (Figure 18), proving that the pollutant and oxygen are not responsible for the decomposition of H_2O_2 and that the decomposition of H_2O_2 occurs with the photoactivated gCN_T catalyst, regardless of the nature of the liquid solution and injected gas.

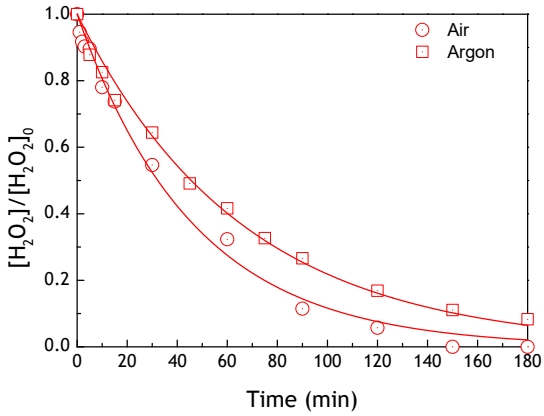

Figure 18. H_2O_2 normalized concentration ($[H_2O_2]/[H_2O_2]_0$), adding H_2O_2 to UP H_2O in the presence of gCN_T and visible light (without model pollutant; experiments #9 & 10 in Table 5).

Comparing Figure 19 (experiment #11, absence of oxygen; k_{app} = 0.004 min^{-1}) and Figure 17 (experiment #6, presence of oxygen; k_{app} = 0.044 min^{-1}), it is interesting to note that a significantly higher k_{app} for the phenol removal was obtained in the presence of oxygen.

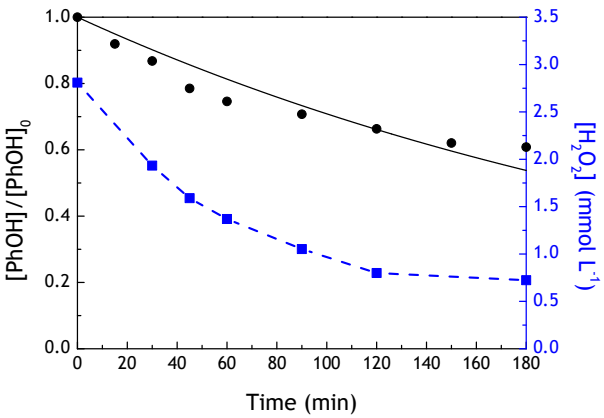

Figure 19. Phenol (normalized) and H_2O_2 concentrations for a photocatalytic experiment with addition of H_2O_2 at t = 0 min, under Ar saturation (experiment #11 in Table 5).

4.2.4 Influence of O_2

As previously mentioned, the H_2O_2 decomposition does not depend on the presence of oxygen, which affects the H_2O_2 formation. The next experiments were conducted to study the influence of this parameter. It was noticed that the irradiation of the LEDs lead to a rise of the temperature inside the reactor. Thus, in a preliminary experiment with UP H_2O and 0.5 g L^{-1} of gCN_T, pure oxygen was bubbled until reaching its saturation in the liquid phase (t = 0 min) and the LEDs were then turned-on (Figure 20). Both DO and temperature were registered and, as expected, the temperature was found to be an important parameter affecting the solubility of oxygen in the liquid phase. After 30 min of irradiation, the temperature starts to stabilize as well as the DO concentration.

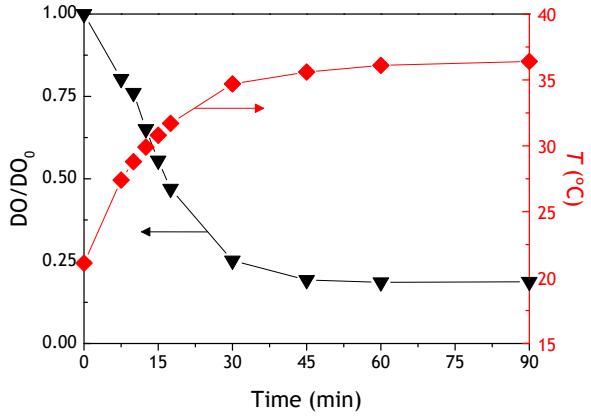

Figure 20. Normalized dissolved oxygen concentration (DO/DO_0) and temperature during irradiation of UP H_2O and after stopping the O_2 flow at t = 0 min (0.50 g L^{-1} catalyst load).

The following run consisted on saturating oxygen in a phenol solution (60 mg L^{-1}). In this case, phenol and the H_2O_2 concentration were also followed (Figure 21). It is possible to identify two stages on the decrease of DO: the first mainly due to the temperature increase (as observed in Figure 20), and the second resulting from the oxygen consumption (probably as a consequence of the H_2O_2 formation). The determined H_2O_2 concentrations are lower than those obtained in the experiments with a constant air saturation (Figure 13). The maximum amount of H_2O_2 retrieved in these assays (ca. 0.05 mmol) is around half of those obtained in standard conditions (ca. 0.10 mmol), i.e. with constant air saturation, as well as a slower degradation of phenol was observed (k_{app} = 0.010 min^{-1} in contrast with k_{app} = 0.033 min^{-1}, respectively). Towards the end of the reaction, the concentration of oxygen stabilizes. This might indicate that the photoactivated electrons are reacting with other compounds, such as intermediate species resulted from phenol degradation.

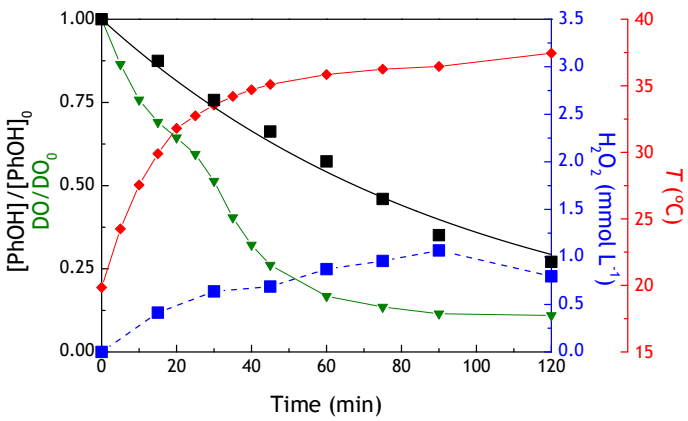

Figure 21. Normalized phenol concentration (–■–, $[PhOH]/[PhOH]_0$), normalized dissolved oxygen concentration (—▼—, DO/DO_0), hydrogen peroxide concentration (- ■ -) and temperature of the solution (—◆—) in the photocatalytic degradation of phenol and after stopping the O_2 flow at t = 0 min (0.50 g L^{-1} catalyst load).

To avoid the effect of the temperature increase on DO, the phenol solution was pre-heated up to nearly 35 ºC (Figure 22), varying less than 3 ºC during the experiment. In this case, the DO decrease is solely due to the formation of H_2O_2. The maximum amount of H_2O_2 reached (0.09 mmol) was close to that obtained in standard conditions (0.10 mmol), but the k_{app} for phenol degradation was still lower (0.015 min^{-1}).

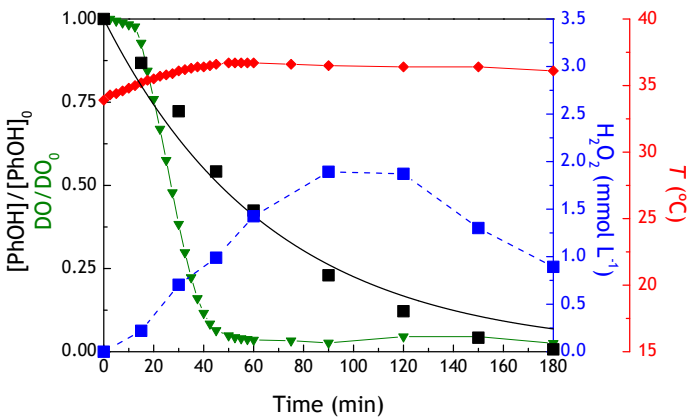

Figure 22. Normalized phenol concentration (—■—, $[PhOH]/[PhOH]_0$), normalized dissolved oxygen concentration (—▼—, DO/DO_0), hydrogen peroxide concentration (- ■ -) and temperature of the solution (—◆—) for an assay performed at higher temperature.

For a better understanding regarding the importance of O_2 in the reactive medium, several assays were performed varying the ratio of oxygen to argon (O_2:Ar) in the gas feed (Figure 23). In general, the DO content initially decreases and then reaches a plateau (Figure 23a) when phenol is completely removed (Figure 23b) (i.e. at 120, 90 and 60 min for 10, 21 and 100% O_2 feeds, respectively). Moreover, a faster phenol degradation is observed in the more O_2-rich solutions (e.g., k_{app} = 0.063 min^{-1} for 100% O_2 and k_{app} = 0.001 min^{-1} for 0% O_2). In terms of H_2O_2 production, H_2O_2 was not detected for 0% O_2, and the highest H_2O_2 amounts of 0.073, 0.082, 0.100 and 0.095 mmol for 5, 10, 21 and 100% O_2 were reached at 180, 150, 120 and 60 min, respectively (Table 6). Thus, in general, higher DO contents lead to higher H_2O_2 amounts in shorter irradiation times (Figure 23c).

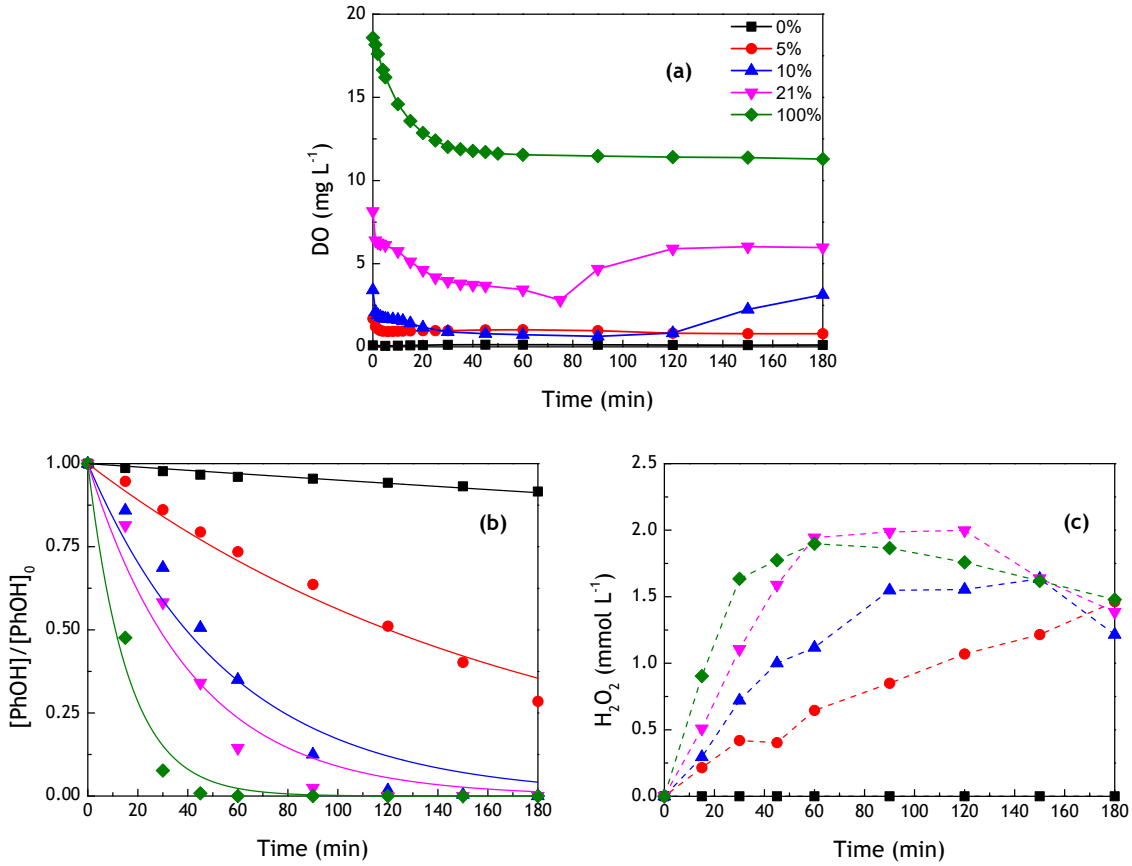

Figure 23. (a) DO content, **(b)** normalized phenol concentration ([PhOH]/[PhOH]$_0$) and **(c)** H_2O_2 concentration in photocatalytic experiments with varying O_2 percentages: 0% (—■—), 5% (—●—), 10% (—▲—), 21% (—▼—), and 100% (—◆—) - at constant pressure: 2 bar).

The pH and TOC content were determined at 180 min (Table 6). The TOC removal, k_{app} and amount of H_2O_2 generally increases with the % O_2, whereas the pH decreases. However, for 21% and 100% of O_2, the amounts of H_2O_2 produced are quite similar. The excess oxygen might be reacting with photoactivated electrons, forming $O_2^{\bullet-}$ radicals, which accelerates the degradation process and explains the similar H_2O_2 evolved amounts.

Table 6. Photocatalytic degradation of phenol varying the percentage of O_2 in the inlet flow.

Flow (% O_2)	TOC removal (%)*	pH*	k_{app} (min^{-1})	H_2O_2 (mmol)
0	3.5	8.41	0.001	0 (—)
5	29.4	7.02	0.006	0.073 (180 min)
10	66.7	5.13	0.018	0.082 (150 min)
21	66.9	4.06	0.024	0.100 (120 min)
100	73.3	3.83	0.063	0.095 (60 min)

* t = 180 min.

4.3 Studies with different aromatic compounds

4.3.1 Selection of probe molecules

A group of several aromatic compounds was chosen for the study of the photocatalytic degradation mechanism using gCN_T, as they are commonly found in phenolic effluents [54-56]. Information about these compounds is organized in Tables 7-9, namely according to their chemical structure together with their pK_a values. The maximum absorption (λ_{max}) and their UV-vis spectra are shown in Appendix C.

Having as starting point the phenol molecule, which has one hydroxyl group (-OH), catechol (CT), resorcinol (RC) and hydroquinone (HQ) were then chosen, these molecules having two hydroxyl groups in the *ortho*, *meta* and *para* positions, respectively (Table 7). This will allow to study the influence of the position of the second hydroxyl group.

Table 7. Chemical structure and pK_a of phenol, catechol (CT), resorcinol (RC) and hydroquinone (HQ).

Compound	Phenol	CT	RC	HQ
Chemical structure	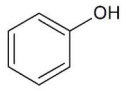	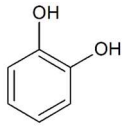	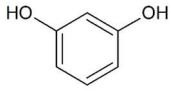	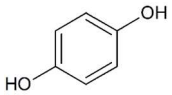
pK_a value	10.0 [57]	9.45 [58]	9.2 [59]	9.9 [60]

Benzoic acid (BA), 4-hydroxybenzoic acid (HBA), protocatechuic acid (PCA) and gallic acid (GA), with none, one, two and three hydroxyl groups, respectively, were also selected (Table 8) to study the influence of the strong electron-donating -OH group, and its position on the ring, over the strong electron-withdrawing -COOH group, as well as the substitution order.

Table 8. Chemical structure and pK_a of benzoic acid (BA), 4-hydroxybenzoic acid (HBA), protocatechuic acid (PCA) and gallic acid (GA).

Compound	BA	HBA	PCA	GA
Chemical structure	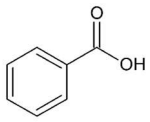	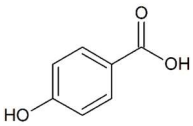	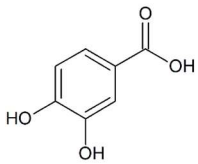	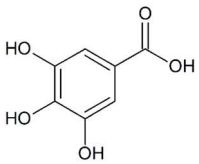
pK_a value	4.19 [61]	4.57 [62]	4.48 [62]	4.40 [63]

4-methoxyphenol (MOP) has a methoxy group, $-OCH_3$, while tyrosol (TYR) has a hydroxyethyl group, $-CH_2CH_2OH$, both in the *para* position (Table 9). A comparison between the model compound without these additional groups (phenol) and these two extra substituents can be thus done, as well as with benzoic acid and hydroquinone. Benzoquinone (BQ) will also be studied as it is a by-product of phenol degradation. Caffeine (CAF) was lastly added to the list since it is an emerging pollutant and has a more complex chemical structure.

Table 9. Chemical structure and pK_a of 4-methoxyphenol (MOP), tyrosol (TYR), caffeine (CAF) and benzoquinone (BQ).

Compound	MOP	TYR	CAF	BQ
Chemical structure	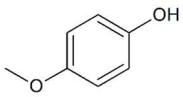	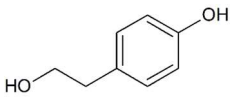	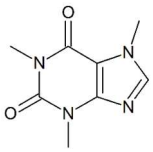	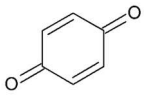
pK_a value	10.2 [57]	10.17 [64]	10.4 [65]	4 [66]

According to the PZC of gCN_T, the material possesses amphoteric properties. Thus, it is expected a quite similar behavior in the presence of more acid or more alkaline compounds, i.e. in terms of the interactions between the molecules and the catalyst surface.

4.3.2 Degradation of probe molecules

All the selected compounds underwent photolytic and photocatalytic reactions. No significant degradation was observed by photolysis, as well as no H_2O_2 was produced (results not shown). Moreover, as expected, no TOC removal was observed by photolysis. Concerning the photocatalytic degradation studies, the first topic discussed in this section is the influence of the position of the hydroxyl group (-OH) on the aromatic ring, in comparison to phenol (PhOH), i.e. CT, RC and HQ (Figure 24). The obtained results are in line with the expected ones, i.e. a faster degradation of resorcinol, then phenol, catechol and hydroquinone (Figure 24 - left). This is due to the activating power of the -OH group which is *ortho* and *para* directing. The RC ring can be easily attacked in three distinct carbon atoms; phenol as well but in a lesser extent. Then, CT and HQ are more difficult to be decomposed since all carbon atoms are less prone to be attacked. PhOH and RC yield the highest amounts of H_2O_2 (Figure 24 – right), as they are the most reactive, achieving the maximum H_2O_2 concentration at 60 min (corresponding to 0.099 and 0.114 mmol of H_2O_2, respectively). CT reaches a maximum of H_2O_2 at 75 min (but only 0.069 mmol) and the H_2O_2 production for HQ increases until 0.073 mmol of H_2O_2 at 180 min of reaction (Figure 24 - left).

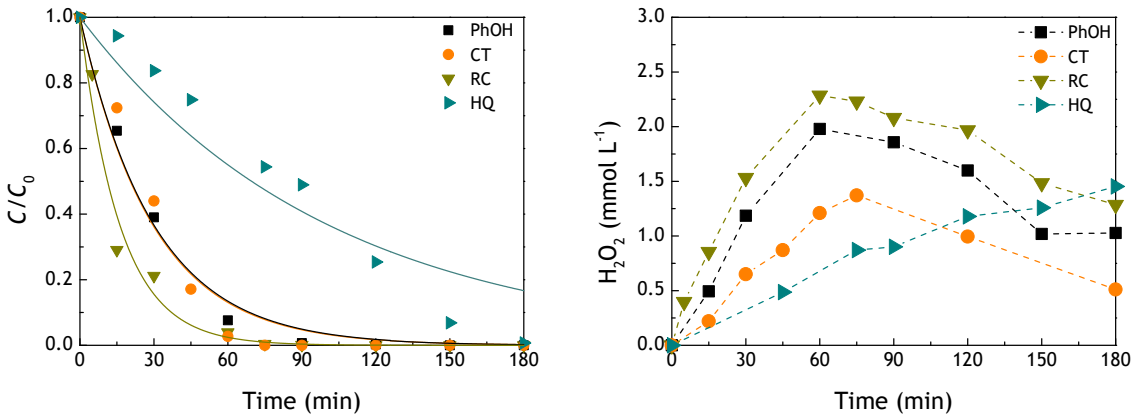

Figure 24. Normalized concentration (left) of phenol (PhOH), catechol (CT), resorcinol (RC) and hydroquinone (HQ) and H_2O_2 production (right) in photocatalytic experiments.

The second topic consists on comparing the four carboxylic acids (BA, HBA, PCA and GA), in this way enabling the analysis of the influence of the number of hydroxyl groups on the ring (Figure 25). As expected, the degradation was faster for GA, then HBA, PCA and lastly BA (Figure 25 - left). The influence of the -OH group is more predominant relatively to the -COOH group, due to their relative strengths. In addition, the presence of more -OH groups can further protect or activate the ring according to their positions. GA is very easily attacked in two positions, as is HBA and PCA although to smaller extents. BA has only one electron-withdrawing group, being the less reactive molecule. All three substituted acids (GA, HBA and PCA) yield high concentrations of H_2O_2 (Figure 25 - right), since they are very reactive molecules that easily donate protons. The more reactive the compound, the higher yield of H_2O_2 obtained. In this case, GA, HBA and PCA showed a maximum H_2O_2 concentration at 90 min (corresponding to 0.140, 0.100 and 0.098 mmol of H_2O_2, respectively). The production of H_2O_2 in the presence of BA is slower, reaching 0.039 mmol of H_2O_2 at 120 min.

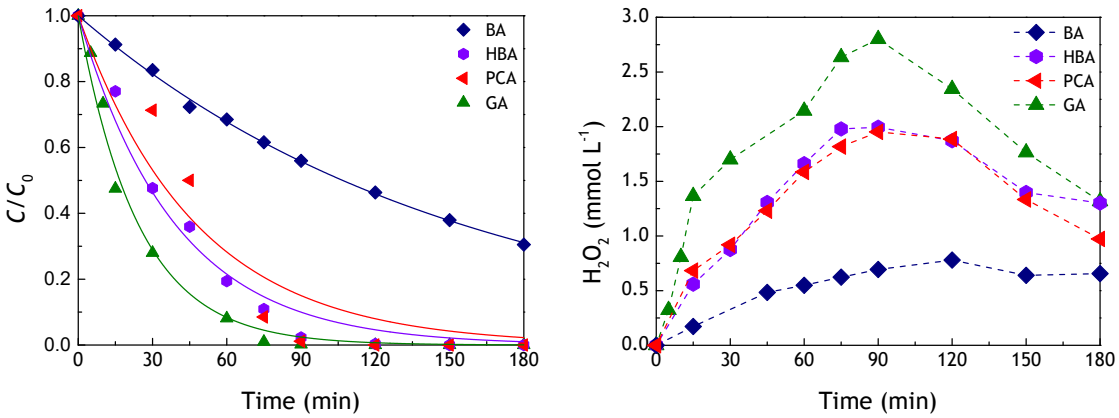

Figure 25. Normalized concentration (left) of benzoic acid (BA), 4-hydroxybenzoic acid (HBA), protocatechuic acid (PCA) and gallic acid (GA) and H_2O_2 production (right) in photocatalytic experiments.

Additionally, a comparison between different *para* substituted aromatic compounds was established with MOP, TYR, BA and HQ. TYR is more easily degraded than MOP and phenol due to the presence of the -OH (*ortho* directing) and $-CH_2CH_2OH$ (*meta* directing) groups, allowing for a greater reactivity with two carbon atoms with more prone tendency to be attacked. Then, MOP has both strong, -OH, and mild, $-OCH_3$, activating groups, resulting in a higher reactivity of the ring. Moreover, PhOH, HQ and BA are increasingly less reactive due to their own *para* substituents (-H, -OH and -COOH, respectively), as previously explained. Lastly, BQ tends to react and be reduced to hydroquinone, its concentration decreasing rapidly (Figure 26 - left). The degradation of CAF (Figure 26 - left) is relatively fast due to tertiary amines inducing more reactivity to this molecule. However, the H^+ are located in amine-neighboring carbon atoms in the caffeine molecule, with relatively high electron-donating ability, yielding a very low production of H_2O_2 (Figure 26 - right). The highest amounts of H_2O_2 produced were 0.092, 0.078, 0.026 and 0.102 mmol at 90, 120, 60 and 180 min, respectively for MOP, TYR, CAF and BQ.

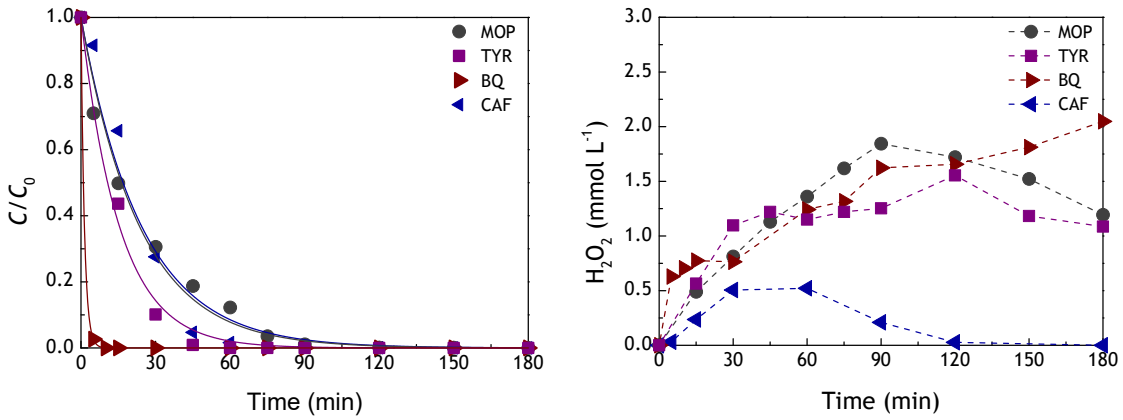

Figure 26. Normalized concentration (left) of 4-methoxyphenol (MOP), tyrosol (TYR), caffeine (CAF) and benzoquinone (BQ) and H_2O_2 production (right) in photocatalytic experiments.

Overall, a general trend can be observed for all aromatic compounds studied: the faster the degradation, the more H_2O_2 is formed. Table 10 summarizes the highest amount of H_2O_2 produced and at which time it was obtained. The degradation rate constant for the aromatic compounds and the TOC removals at the end of the reaction are also presented.

Table 10. Highest amount of H_2O_2 produced, apparent first-order rate constant (k_{app}) and TOC removal after photocatalysis of all selected compounds.

Compound	Highest H_2O_2 amount (mmol) (at time (min))	k_{app} (min^{-1})	TOC removal (%)
Phenol	0.099 (60)	0.034	76.3
Catechol	0.069 (75)	0.034	77.8
Resorcinol	0.114 (60)	0.062	76.8
Hydroquinone	0.073 (180)	0.010	69.3
Benzoic acid	0.039 (120)	0.007	46.0
4-Hydroxybenzoic acid	0.100 (90)	0.026	77.7
Protocatechuic acid	0.098 (90)	0.021	72.9
Gallic acid	0.140 (90)	0.041	71.0
4-Methoxyphenol	0.092 (90)	0.043	52.1
Tyrosol	0.078 (120)	0.065	43.4
Caffeine	0.026 (60)	0.041	11.7
Benzoquinone	0.102 (180)	0.726	63.5

As previously explained, some compounds tend to be more easily attacked than others. This can be demonstrated by the k_{app} values listed in Table 10. Moreover, the TOC removals were above 70% in many cases, except for the more recalcitrant compounds. As referred before, the carbon content remaining in the solution has a small contribution from some catalyst particles which were not retained by filtration of the liquid samples (Table 3). However, the main contributors to the TOC content are aliphatic acids which comprehend the final oxidation products. The pH at the end of the reactions are in agreement with this hypothesis, yielding values below 4 and, thus, meaning that the solution contains such acids.

In terms of the highest H_2O_2 production rates, resorcinol, phenol and gallic acid lead to 4570, 4741 and 6552 μmol g_{cat}^{-1} h^{-1}, respectively. In comparison with other reports, described in Section 2.3, the H_2O_2 production rates obtained in the framework of the present dissertation (as well as the amount of H_2O_2) are much higher than those previously reported using other g-C_3N_4 materials. For comparison, the highest H_2O_2 production rate previously obtained was 3300 μmol g_{cat}^{-1} h^{-1}, and the highest amount of H_2O_2 was 0.130 mmol after 24 h (Table 2). Since gallic acid was the compound generating the highest amount of H_2O_2 (0.140 mmol in 90 min), this compound was selected to perform a longer photocatalytic experiment (Figure 27). From this experiment it is clearly noted that the H_2O_2 concentration increases up to 90 min (as also observed in Figure 25 - right) and then decreases gradually until being nearly completely consumed.

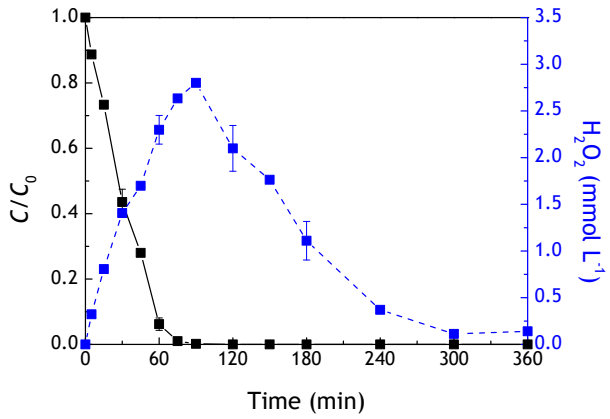

Figure 27. Photocatalytic degradation of gallic acid and H_2O_2 concentration evolution.

4.3.3 pK_a possible effect on the degradation of aromatic compounds and H_2O_2 production

To investigate the possible influence of the pK_a of the studied compounds, the degradation rate constants of these aromatic compounds (Figure 28 - left) and respective TOC removals achieved at 180 min (Figure 28 - right) were compared (positioning phenol at the left of each figure and then the other compounds from the most to least acidic). However, correlations between pK_a

and these results were not found. The type, number and position of substituent groups on the aromatic ring are more determinant factors, as previously discussed.

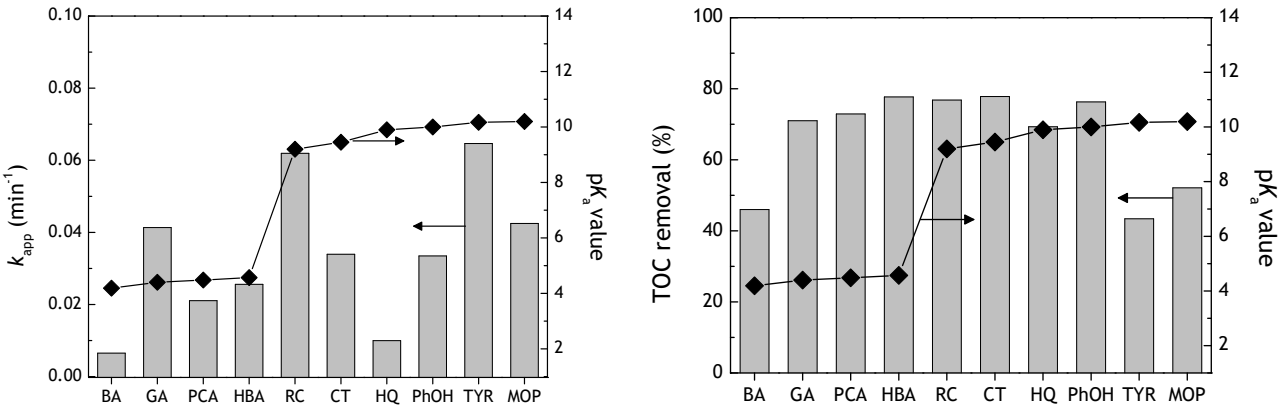

Figure 28. Degradation kinetic constant (left) and TOC removal (right) according to the pK_a for the studied aromatic compounds.

Likewise, the pK_a does not affect the H_2O_2 production (Figure 29), which is mainly influenced by the DO content and the presence of more -OH groups in the ring. These observations are in agreement with the amphoteric properties of gCN_T.

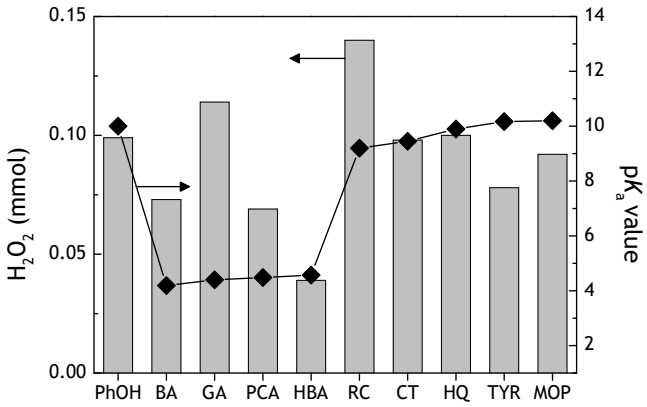

Figure 29. H_2O_2 production according to the pK_a for the studied aromatic compounds.

5 Conclusions

The representative conclusions of this dissertation are summarized as follows:

- Most of the studied aromatic compounds were oxidized to levels below the limit of quantification in less than 3 h, with simultaneous H_2O_2 production under visible light and employing a metal-free gCN_T photocatalyst load (0.5 g L^{-1}) that was optimized for the degradation of phenol;
- H_2O_2 is formed in the presence of photoactivated gCN_T, oxygen and a proton donor (the model pollutant), and decomposed with photoactivated gCN_T dispersed in water;
- The highest amount of H_2O_2 and production rate obtained with gCN_T and gallic acid (0.140 mmol at 90 min and 6552 μmol g_{cat}^{-1} h^{-1}, respectively) were considerably superior than those reported in the literature for other g-C_3N_4 photocatalysts (0.130 mmol at 24 h and 3300 μmol g_{cat}^{-1} h^{-1});
- The position, nature and order of aromatic ring substituents strongly affect the degradation of the studied aromatic compounds, and generally higher amounts of H_2O_2 are obtained for the most reactive molecules;
- Correlations between the pK_a of the aromatic compounds and their degradation rates, TOC removals and H_2O_2 productions were not found, in agreement with the amphoteric properties of gCN_T.

Thus, the main objective of this dissertation was achieved, since a system implementing a metal-free catalyst and visible light was demonstrated for the degradation of aromatic compounds and simultaneous H_2O_2 production in aqueous solutions, with a better understanding of the mechanisms involved.

6 Assessment of the work done

The degradation of organic pollutants using g-C_3N_4 as photocatalyst has been a hot topic of research in recent years, with several studies reporting modifications towards improved photocatalytic activity. In this work, the main goal was achieved, but more studies are needed to fully understand these mechanisms as well as the degradation pathways of the studied compounds. One current experimental limitation is the impossibility to identify the different ROS that are generated in this photocatalytic system.

6.1 Objectives achieved

As mentioned above, the main objective of this dissertation was achieved, namely the gCN_T metal-free catalyst was active under visible light for the degradation of aromatic compounds and simultaneous H_2O_2 production in aqueous solutions. In terms of the mechanisms involved, new insights were gained concerning the formation and decomposition of H_2O_2. Moreover, the studies performed regarding the degradation of several aromatic compounds allowed to comprehend the impact of the substitution nature, position and order.

6.2 Other work carried out

Four poster communications resulted from this dissertation:

1. **A. Torres-Pinto**, M.J. Sampaio, C.G. Silva, J.L. Faria, A.M.T. Silva, "Visible-light degradation of aromatic pollutants using exfoliated graphitic carbon nitride as photocatalyst", *8th International Symposium on Carbon for Catalysis*, June 26-29, 2018.

2. **A. Torres-Pinto**, M.J. Sampaio, C.G. Silva, J.L. Faria, A.M.T. Silva, "Visible-light degradation of aromatic pollutants using exfoliated graphitic carbon nitride as photocatalyst", *3rd International Conference on New Photocatalytic Materials for Environment, Energy and Sustainability and 4th International Conference on Photocatalytic and Advanced Oxidation Technologies for the Treatment of Water, Air, Soil and Surfaces*, Porto, July 10-13, 2018.

3. **A. Torres-Pinto**, M.J. Sampaio, C.G. Silva, J.L. Faria, A.M.T. Silva, "Degradação de poluentes aromáticos com um fotocatalisador de nitreto de carbono grafítico exfoliado e ativado por radiação visível", to be presented at the *Escola Ibero-Americana de Catálise*, Lisboa, September 7, 2018.

4. **A. Torres-Pinto**, M.J. Sampaio, C.G. Silva, J.L. Faria, A.M.T. Silva, "Exfoliated graphitic carbon nitride for photocatalytic degradation of aromatic contaminants with simultaneous production of H_2O_2", to be presented at the *VIth Jornadas Ibéricas de Fotoquímica,* Aveiro, September 12-14, 2018.

6.3 Limitations and future work

The most significant limitation found on this work was the impossibility to directly quantify the concentration of radical species. Thus, a HPLC fluorescence detection method could be developed and optimized in the future. Moreover, photocatalytic experiments using radical scavengers, i.e. ROS trapping experiments, could be performed, aiming at the establishment of correlations between the abatement of the studied pollutants and the respective H_2O_2 productions.

Other proposed future tasks are: (i) to repeat some experiments in order to determine the experimental errors; (ii) to reuse the catalyst in consecutive experiments; (iii) to immobilize the catalyst on an appropriate support; and (iv) to perform experiments with real waste waters envisaging future full-scale applications. It would be also interesting to modify the g-C_3N_4 material by other approaches, such as metal-free doping and/or other post-treatments, aiming to improve the degradation of pollutants and H_2O_2 production and in this way expanding the possibilities for the applications of this material.

References

[1] A.R. Ribeiro, O.C. Nunes, M.F.R. Pereira, A.M.T. Silva, An overview on the advanced oxidation processes applied for the treatment of water pollutants defined in the recently launched Directive 2013/39/EU, Environment International, 75 (2015) 33-51.

[2] A. Buthiyappan, R. Abdul Aziz Abdul, A. Wan Daud Wan Mohd, Recent advances and prospects of catalytic advanced oxidation process in treating textile effluents, Reviews in Chemical Engineering, 32 (2016) 1-47.

[3] C. J. Philippopoulos, M. D Nikolaki, Photocatalytic Processes on the Oxidation of Organic Compounds in Water, 2010.

[4] Y. Deng, R. Zhao, Advanced Oxidation Processes (AOPs) in Wastewater Treatment, Current Pollution Reports, 1 (2015) 167-176.

[5] X. Li, J. Yu, M. Jaroniec, Hierarchical photocatalysts, Chemical Society Reviews, 45 (2016) 2603-2636.

[6] H. Li, Z. Bian, J. Zhu, Y. Huo, H. Li, Y. Lu, Mesoporous Au/TiO_2 Nanocomposites with Enhanced Photocatalytic Activity, Journal of the American Chemical Society, 129 (2007) 4538-4539.

[7] J.H. Pan, X. Zhang, A.J. Du, D.D. Sun, J.O. Leckie, Self-Etching Reconstruction of Hierarchically Mesoporous F-TiO_2 Hollow Microspherical Photocatalyst for Concurrent Membrane Water Purifications, Journal of the American Chemical Society, 130 (2008) 11256-11257.

[8] W.-J. Ong, L.-L. Tan, Y.H. Ng, S.-T. Yong, S.-P. Chai, Graphitic Carbon Nitride (g-C_3N_4)-Based Photocatalysts for Artificial Photosynthesis and Environmental Remediation: Are We a Step Closer To Achieving Sustainability?, Chemical Reviews, 116 (2016) 7159-7329.

[9] S. Liu, D. Li, H. Sun, H.M. Ang, M.O. Tadé, S. Wang, Oxygen functional groups in graphitic carbon nitride for enhanced photocatalysis, Journal of Colloid and Interface Science, 468 (2016) 176-182.

[10] G. Wu, S. Hu, Z. Han, C. Liu, Q. Li, The effect of Ni(i)-N active sites on the photocatalytic H_2O_2 production ability over nickel doped graphitic carbon nitride nanofibers, New Journal of Chemistry, 41 (2017) 15289-15297.

[11] Y. Cui, Z. Ding, P. Liu, M. Antonietti, X. Fu, X. Wang, Metal-free activation of H_2O_2 by g-C_3N_4 under visible light irradiation for the degradation of organic pollutants, Physical Chemistry Chemical Physics, 14 (2012) 1455-1462.

[12] N. Barbero, D. Vione, Why Dyes Should Not Be Used to Test the Photocatalytic Activity of Semiconductor Oxides, Environmental Science & Technology, 50 (2016) 2130-2131.

[13] M. Mehrjouei, S. Müller, D. Möller, A review on photocatalytic ozonation used for the treatment of water and wastewater, Chemical Engineering Journal, 263 (2015) 209-219.

[14] H. Wang, Y. Su, H. Zhao, H. Yu, S. Chen, Y. Zhang, X. Quan, Photocatalytic oxidation of aqueous ammonia using atomic single layer graphitic-C_3N_4, Environmental Science and Technology, 48 (2014) 11984-11990.

[15] P. Qiu, C. Xu, H. Chen, F. Jiang, X. Wang, R. Lu, X. Zhang, One step synthesis of oxygen doped porous graphitic carbon nitride with remarkable improvement of photo-oxidation activity: Role of oxygen on visible light photocatalytic activity, Applied Catalysis B: Environmental, 206 (2017) 319-327.

[16] G. Liao, D. Zhu, L. Li, B. Lan, Enhanced photocatalytic ozonation of organics by g-C_3N_4 under visible light irradiation, Journal of Hazardous Materials, 280 (2014) 531-535.

[17] Y. Cui, J. Huang, X. Fu, X. Wang, Metal-free photocatalytic degradation of 4-chlorophenol in water by mesoporous carbon nitride semiconductors, Catalysis Science and Technology, 2 (2012) 1396-1402.

[18] A. Kumar, A. Kumar, G. Sharma, M. Naushad, R.C. Veses, A.A. Ghfar, F.J. Stadler, M.R. Khan, Solar-driven photodegradation of 17-ß-estradiol and ciprofloxacin from waste water and

CO_2 conversion using sustainable coal-char/polymeric-g-C_3N_4/rGO metal-free nano-hybrids, New Journal of Chemistry, 41 (2017) 10208-10224.

[19] Q. Wu, Y. He, H. Zhang, Z. Feng, Y. Wu, T. Wu, Photocatalytic selective oxidation of biomass-derived 5-hydroxymethylfurfural to 2,5-diformylfuran on metal-free g-C_3N_4 under visible light irradiation, Molecular Catalysis, 436 (2017) 10-18.

[20] X. Liu, X. Wu, Z. Long, C. Zhang, Y. Ma, X. Hao, H. Zhang, C. Pan, Photodegradation of Imidacloprid in Aqueous Solution by the Metal-Free Catalyst Graphitic Carbon Nitride using an Energy-Saving Lamp, Journal of Agricultural and Food Chemistry, 63 (2015) 4754-4760.

[21] J. Xiao, Y. Xie, H. Cao, Y. Wang, Z. Guo, Y. Chen, Towards effective design of active nanocarbon materials for integrating visible-light photocatalysis with ozonation, Carbon, 107 (2016) 658-666.

[22] J. Yin, G. Liao, D. Zhu, P. Lu, L. Li, Photocatalytic ozonation of oxalic acid by g-C_3N_4/graphene composites under simulated solar irradiation, Journal of Photochemistry and Photobiology A: Chemistry, 315 (2016) 138-144.

[23] W. Ding, S. Liu, Z. He, One-step synthesis of graphitic carbon nitride nanosheets for efficient catalysis of phenol removal under visible light, Cuihua Xuebao/Chinese Journal of Catalysis, 38 (2017) 1711-1718.

[24] S. Liu, J. Ke, H. Sun, J. Liu, M.O. Tade, S. Wang, Size dependence of uniformed carbon spheres in promoting graphitic carbon nitride toward enhanced photocatalysis, Applied Catalysis B: Environmental, 204 (2017) 358-364.

[25] C. Zhou, C. Lai, D. Huang, G. Zeng, C. Zhang, M. Cheng, L. Hu, J. Wan, W. Xiong, M. Wen, X. Wen, L. Qin, Highly porous carbon nitride by supramolecular preassembly of monomers for photocatalytic removal of sulfamethazine under visible light driven, Applied Catalysis B: Environmental, 220 (2018) 202-210.

[26] H. Lan, L. Li, X. An, F. Liu, C. Chen, H. Liu, J. Qu, Microstructure of carbon nitride affecting synergetic photocatalytic activity: Hydrogen bonds vs. structural defects, Applied Catalysis B: Environmental, 204 (2017) 49-57.

[27] H. Lan, L. Li, H. Liu, X. An, F. Liu, C. Chen, J. Qu, Melem-based derivatives as metal-free photocatalysts for simultaneous reduction of Cr(VI) and degradation of 5-Sulfosalicylic acid, Journal of Colloid and Interface Science, 507 (2017) 162-171.

[28] L. Jiang, X. Yuan, G. Zeng, Z. Wu, J. Liang, X. Chen, L. Leng, H. Wang, H. Wang, Metal-free efficient photocatalyst for stable visible-light photocatalytic degradation of refractory pollutant, Applied Catalysis B: Environmental, 221 (2018) 715-725.

[29] Y. Kofuji, S. Ohkita, Y. Shiraishi, H. Sakamoto, S. Tanaka, S. Ichikawa, T. Hirai, Graphitic Carbon Nitride Doped with Biphenyl Diimide: Efficient Photocatalyst for Hydrogen Peroxide Production from Water and Molecular Oxygen by Sunlight, ACS Catalysis, 6 (2016) 7021-7029.

[30] Y. Shiraishi, Y. Kofuji, H. Sakamoto, S. Tanaka, S. Ichikawa, T. Hirai, Effects of Surface Defects on Photocatalytic H_2O_2 Production by Mesoporous Graphitic Carbon Nitride under Visible Light Irradiation, ACS Catalysis, 5 (2015) 3058-3066.

[31] H. Zhang, L.-H. Guo, L. Zhao, B. Wan, Y. Yang, Switching Oxygen Reduction Pathway by Exfoliating Graphitic Carbon Nitride for Enhanced Photocatalytic Phenol Degradation, The Journal of Physical Chemistry Letters, 6 (2015) 958-963.

[32] Y. Shiraishi, S. Kanazawa, Y. Sugano, D. Tsukamoto, H. Sakamoto, S. Ichikawa, T. Hirai, Highly selective production of hydrogen peroxide on graphitic carbon nitride (g-C_3N_4) photocatalyst activated by visible light, ACS Catalysis, 4 (2014) 774-780.

[33] Y. Yao, G. Wu, F. Lu, S. Wang, Y. Hu, J. Zhang, W. Huang, F. Wei, Enhanced photo-Fenton-like process over Z-scheme $CoFe_2O4$/g-C_3N_4 Heterostructures under natural indoor light, Environmental Science and Pollution Research, 23 (2016) 21833-21845.

[34] W. Li, D. Li, Y. Lin, P. Wang, W. Chen, X. Fu, Y. Shao, Evidence for the Active Species Involved in the Photodegradation Process of Methyl Orange on TiO_2, The Journal of Physical Chemistry C, 116 (2012) 3552-3560.

[35] Y. Shiraishi, S. Kanazawa, Y. Kofuji, H. Sakamoto, S. Ichikawa, S. Tanaka, T. Hirai, Sunlight-driven hydrogen peroxide production from water and molecular oxygen by metal-free photocatalysts, Angewandte Chemie - International Edition, 53 (2014) 13454-13459.

[36] Y. Kofuji, S. Ohkita, Y. Shiraishi, H. Sakamoto, S. Ichikawa, S. Tanaka, T. Hirai, Mellitic Triimide-Doped Carbon Nitride as Sunlight-Driven Photocatalysts for Hydrogen Peroxide Production, ACS Sustainable Chemistry and Engineering, 5 (2017) 6478-6485.

[37] S. Zhao, T. Guo, X. Li, T. Xu, B. Yang, X. Zhao, Carbon nanotubes covalent combined with graphitic carbon nitride for photocatalytic hydrogen peroxide production under visible light, Applied Catalysis B: Environmental, 224 (2018) 725-732.

[38] S. Li, G. Dong, R. Hailili, L. Yang, Y. Li, F. Wang, Y. Zeng, C. Wang, Effective photocatalytic H_2O_2 production under visible light irradiation at g-C_3N_4 modulated by carbon vacancies, Applied Catalysis B: Environmental, 190 (2016) 26-35.

[39] L. Yang, G. Dong, D.L. Jacobs, Y. Wang, L. Zang, C. Wang, Two-channel photocatalytic production of H_2O_2 over g-C_3N_4 nanosheets modified with perylene imides, Journal of Catalysis, 352 (2017) 274-281.

[40] L. Svoboda, P. Praus, M.J. Lima, M.J. Sampaio, D. Matýsek, M. Ritz, R. Dvorský, J.L. Faria, C.G. Silva, Graphitic carbon nitride nanosheets as highly efficient photocatalysts for phenol degradation under high-power visible LED irradiation, Materials Research Bulletin, 100 (2018) 322-332.

[41] M.J. Lima, A.M.T. Silva, C.G. Silva, J.L. Faria, Graphitic carbon nitride modified by thermal, chemical and mechanical processes as metal-free photocatalyst for the selective synthesis of benzaldehyde from benzyl alcohol, Journal of Catalysis, 353 (2017) 44-53.

[42] M.J. Sampaio, R.R. Bacsa, A. Benyounes, R. Axet, P. Serp, C.G. Silva, A.M.T. Silva, J.L. Faria, Synergistic effect between carbon nanomaterials and ZnO for photocatalytic water decontamination, Journal of Catalysis, 331 (2015) 172-180.

[43] J.-M. Herrmann, Titania-based true heterogeneous photocatalysis, Environmental Science and Pollution Research, 19 (2012) 3655-3665.

[44] M.J. Sampaio, C.G. Silva, A.M.T. Silva, J.L. Faria, Kinetic modelling for the photocatalytic degradation of phenol by using TiO_2-coated glass raschig rings under simulated solar light, Journal of Chemical Technology and Biotechnology, 91 (2016) 346-352.

[45] J.L. Figueiredo, Functionalization of porous carbons for catalytic applications, Journal of Materials Chemistry A, 1 (2013) 9351-9364.

[46] P. Xia, B. Zhu, J. Yu, S. Cao, M. Jaroniec, Ultra-thin nanosheet assemblies of graphitic carbon nitride for enhanced photocatalytic CO_2 reduction, Journal of Materials Chemistry A, 5 (2017) 3230-3238.

[47] B. Zhu, P. Xia, W. Ho, J. Yu, Isoelectric point and adsorption activity of porous g-C_3N_4, Applied Surface Science, 344 (2015) 188-195.

[48] M. Fronczak, M. Krajewska, K. Demby, M. Bystrzejewski, Extraordinary Adsorption of Methyl Blue onto Sodium-Doped Graphitic Carbon Nitride, The Journal of Physical Chemistry C, 121 (2017) 15756-15766.

[49] J. Li, Y. Liu, H. Li, C. Chen, Fabrication of g-C_3N_4/TiO_2 composite photocatalyst with extended absorption wavelength range and enhanced photocatalytic performance, Journal of Photochemistry and Photobiology A: Chemistry, 317 (2016) 151-160.

[50] A. Armstrong David, E. Huie Robert, H. Koppenol Willem, V. Lymar Sergei, G. Merényi, P. Neta, B. Ruscic, M. Stanbury David, S. Steenken, P. Wardman, Standard electrode potentials involving radicals in aqueous solution: inorganic radicals (IUPAC Technical Report), in: Pure and Applied Chemistry, 2015, pp. 1139.

[51] J.P. Collman, P. Denisevich, Y. Konai, M. Marrocco, C. Koval, F.C. Anson, Electrode catalysis of the four-electron reduction of oxygen to water by dicobalt face-to-face porphyrins, Journal of the American Chemical Society, 102 (1980) 6027-6036.

[52] J.J. Guerard, P.R. Tentscher, M. Seijo, J. Samuel Arey, Explicit solvent simulations of the aqueous oxidation potential and reorganization energy for neutral molecules: gas phase, linear solvent response, and non-linear response contributions, Physical Chemistry Chemical Physics, 17 (2015) 14811-14826.

[53] A.I.R. Morgado, Structured carbon materials for wastewater treatment, in: Associate Laboratory LSRE-LCM, Faculty of Engineering of University of Porto, 2017.

[54] M.J. Sampaio, C.G. Silva, A.M.T. Silva, V.J.P. Vilar, R.A.R. Boaventura, J.L. Faria, Photocatalytic activity of TiO_2-coated glass raschig rings on the degradation of phenolic derivatives under simulated solar light irradiation, Chemical Engineering Journal, 224 (2013) 32-38.

[55] A.M.T. Silva, E. Nouli, N.P. Xekoukoulotakis, D. Mantzavinos, Effect of key operating parameters on phenols degradation during H_2O_2-assisted TiO_2 photocatalytic treatment of simulated and actual olive mill wastewaters, Applied Catalysis B: Environmental, 73 (2007) 11-22.

[56] A.M.T. Silva, E. Nouli, Â.C. Carmo-Apolinário, N.P. Xekoukoulotakis, D. Mantzavinos, Sonophotocatalytic/H_2O_2 degradation of phenolic compounds in agro-industrial effluents, Catalysis Today, 124 (2007) 232-239.

[57] W. Reusch, Acidity of Substituted Phenols, in, MindTouch, 2014.

[58] E.P.D. Serjeant, Boyd, Ionisation constants of organic acids in aqueous solution, Pergamon Press, Oxford; New York, 1979.

[59] S.E. Blanco, M.C. Almandoz, F.H. Ferretti, Determination of the overlapping pKa values of resorcinol using UV-visible spectroscopy and DFT methods, Spectrochimica Acta Part A: Molecular and Biomolecular Spectroscopy, 61 (2005) 93-102.

[60] Technical data bulletin, in, Eastman Chemical Products, Inc., 1975.

[61] C.A. Hollingsworth, P.G. Seybold, C.M. Hadad, Substituent effects on the electronic structure and pK_a of benzoic acid, International Journal of Quantum Chemistry, 90 (2002) 1396-1403.

[62] W.M. Haynes, CRC Handbook of Chemistry and Physics, 97th Edition, CRC Press, 2016.

[63] F.A. Patty, Industrial Hygiene and Toxicology. Vol. II. 2nd rev. ed., Journal of Pharmaceutical Sciences, 52 916.

[64] U. Urzúa, Fenoles y aminas, in, Facultad de Medicina, Universidad de Chile, 2009.

[65] J.A. Dean, Lange's handbook of chemistry, 14 ed., McGraw-Hill, 1992.

[66] R. Hasegawa, K. Saito, T. Takaoka, H. Ishikita, pK_a of ubiquinone, menaquinone, phylloquinone, plastoquinone, and rhodoquinone in aqueous solution, Photosynthesis Research, 133 (2017) 297-304.

[67] G. Mamba, A.K. Mishra, Graphitic carbon nitride (g-C_3N_4) nanocomposites: A new and exciting generation of visible light driven photocatalysts for environmental pollution remediation, Applied Catalysis B: Environmental, 198 (2016) 347-377.

[68] F. Raziq, C. Li, M. Humayun, Y. Qu, A. Zada, H. Yu, L. Jing, Synthesis of TiO_2/g-C_3N_4 nanocomposites as efficient photocatalysts dependent on the enhanced photogenerated charge separation, Materials Research Bulletin, 70 (2015) 494-499.

[69] K.-i. Katsumata, R. Motoyoshi, N. Matsushita, K. Okada, Preparation of graphitic carbon nitride (g-C_3N_4)/WO_3 composites and enhanced visible-light-driven photodegradation of acetaldehyde gas, Journal of Hazardous Materials, 260 (2013) 475-482.

[70] D. Masih, Y. Ma, S. Rohani, Graphitic C_3N_4 based noble-metal-free photocatalyst systems: A review, Applied Catalysis B: Environmental, 206 (2017) 556-588.

[71] J. Xia, M. Ji, J. Di, B. Wang, S. Yin, Q. Zhang, M. He, H. Li, Construction of ultrathin $C_3N_4/Bi_4O_5I_2$ layered nanojunctions via ionic liquid with enhanced photocatalytic performance and mechanism insight, Applied Catalysis B: Environmental, 191 (2016) 235-245.

[72] P. Qiu, H. Chen, F. Jiang, Cobalt modified mesoporous graphitic carbon nitride with enhanced visible-light photocatalytic activity, RSC Advances, 4 (2014) 39969-39977.

[73] H.-P. Lin, C.-C. Chen, W.W. Lee, Y.-Y. Lai, J.-Y. Chen, Y.-Q. Chen, J.-Y. Fu, Synthesis of a $SrFeO_{3-x}/g\text{-}C_3N_4$ heterojunction with improved visible-light photocatalytic activities in chloramphenicol and crystal violet degradation, RSC Advances, 6 (2016) 2323-2336.

[74] S. Kumar, A. Kumar, A. Bahuguna, V. Sharma, V. Krishnan, Two-dimensional carbon-based nanocomposites for photocatalytic energy generation and environmental remediation applications, Beilstein Journal of Nanotechnology, 8 (2017) 1571-1600.

[75] S. Kumar, S. Tonda, A. Baruah, B. Kumar, V. Shanker, Synthesis of novel and stable $g\text{-}C_3N_4$/N-doped $SrTiO_3$ hybrid nanocomposites with improved photocurrent and photocatalytic activity under visible light irradiation, Dalton Transactions, 43 (2014) 16105-16114.

[76] Z. Jiang, C. Zhu, W. Wan, K. Qian, J. Xie, Constructing graphite-like carbon nitride modified hierarchical yolk-shell TiO2 spheres for water pollution treatment and hydrogen production, Journal of Materials Chemistry A, 4 (2016) 1806-1818.

[77] Z. Zhu, Z. Lu, X. Zhao, Y. Yan, W. Shi, D. Wang, L. Yang, X. Lin, Z. Hua, Y. Liu, Surface imprinting of a $g\text{-}C_3N_4$ photocatalyst for enhanced photocatalytic activity and selectivity towards photodegradation of 2-mercaptobenzothiazole, RSC Advances, 5 (2015) 40726-40736.

[78] W. Chen, T.-Y. Liu, T. Huang, X.-H. Liu, X.-J. Yang, Novel mesoporous P-doped graphitic carbon nitride nanosheets coupled with $ZnIn_2S_4$ nanosheets as efficient visible light driven heterostructures with remarkably enhanced photo-reduction activity, Nanoscale, 8 (2016) 3711-3719.

[79] H. Wang, X. Yuan, H. Wang, X. Chen, Z. Wu, L. Jiang, W. Xiong, Y. Zhang, G. Zeng, One-step calcination method for synthesis of mesoporous $g\text{-}C_3N_4/NiTiO_3$ heterostructure photocatalyst with improved visible light photoactivity, RSC Advances, 5 (2015) 95643-95648.

[80] Y. Yang, Y. Guo, F. Liu, X. Yuan, Y. Guo, S. Zhang, W. Guo, M. Huo, Preparation and enhanced visible-light photocatalytic activity of silver deposited graphitic carbon nitride plasmonic photocatalyst, Applied Catalysis B: Environmental, 142-143 (2013) 828-837.

[81] W. Raza, D. Bahnemann, M. Muneer, Efficient visible light driven, mesoporous graphitic carbon nitrite based hybrid nanocomposite: With superior photocatalytic activity for degradation of organic pollutant in aqueous phase, Journal of Photochemistry and Photobiology A: Chemistry, 342 (2017) 102-115.

[82] M. Xu, L. Han, S. Dong, Facile Fabrication of Highly Efficient $g\text{-}C_3N_4/Ag_2O$ Heterostructured Photocatalysts with Enhanced Visible-Light Photocatalytic Activity, ACS Applied Materials & Interfaces, 5 (2013) 12533-12540.

[83] X. Bai, L. Wang, Y. Wang, W. Yao, Y. Zhu, Enhanced oxidation ability of $g\text{-}C_3N_4$ photocatalyst via C_{60} modification, Applied Catalysis B: Environmental, 152-153 (2014) 262-270.

[84] H. Liu, Z. Jin, Z. Xu, Hybridization of $Cd_{0.2}Zn_{0.8}S$ with $g\text{-}C_3N_4$ nanosheets: a visible-light-driven photocatalyst for H2 evolution from water and degradation of organic pollutants, Dalton Transactions, 44 (2015) 14368-14375.

[85] L. Jiang, X. Yuan, Y. Pan, J. Liang, G. Zeng, Z. Wu, H. Wang, Doping of graphitic carbon nitride for photocatalysis: A reveiw, Applied Catalysis B: Environmental, 217 (2017) 388-406.

[86] M. Zhang, X. Bai, D. Liu, J. Wang, Y. Zhu, Enhanced catalytic activity of potassium-doped graphitic carbon nitride induced by lower valence position, Applied Catalysis B: Environmental, 164 (2015) 77-81.

[87] Y. He, L. Zhang, M. Fan, X. Wang, M.L. Walbridge, Q. Nong, Y. Wu, L. Zhao, Z-scheme $SnO_{2-x}/g\text{-}C_3N_4$ composite as an efficient photocatalyst for dye degradation and photocatalytic CO_2 reduction, Solar Energy Materials and Solar Cells, 137 (2015) 175-184.

[88] Z. Zhang, J. Huang, M. Zhang, Q. Yuan, B. Dong, Ultrathin hexagonal SnS_2 nanosheets coupled with g-C_3N_4 nanosheets as 2D/2D heterojunction photocatalysts toward high photocatalytic activity, Applied Catalysis B: Environmental, 163 (2015) 298-305.

[89] H. Li, L. Zhou, L. Wang, Y. Liu, J. Lei, J. Zhang, In situ growth of TiO_2 nanocrystals on g-C_3N_4 for enhanced photocatalytic performance, Physical Chemistry Chemical Physics, 17 (2015) 17406-17412.

[90] Y. Li, J. Wang, Y. Yang, Y. Zhang, D. He, Q. An, G. Cao, Seed-induced growing various TiO_2 nanostructures on g-C_3N_4 nanosheets with much enhanced photocatalytic activity under visible light, Journal of Hazardous Materials, 292 (2015) 79-89.

[91] J. Yao, H. Chen, F. Jiang, Z. Jiao, M. Jin, Titanium dioxide and cadmium sulfide co-sensitized graphitic carbon nitride nanosheets composite photocatalysts with superior performance in phenol degradation under visible-light irradiation, Journal of Colloid and Interface Science, 490 (2017) 154-162.

[92] H. Liu, Z. Jin, Z. Xu, Z. Zhang, D. Ao, Fabrication of $ZnIn_2S_4$-g-C_3N_4 sheet-on-sheet nanocomposites for efficient visible-light photocatalytic H2-evolution and degradation of organic pollutants, RSC Advances, 5 (2015) 97951-97961.

[93] Z. Zhu, Z. Lu, D. Wang, X. Tang, Y. Yan, W. Shi, Y. Wang, N. Gao, X. Yao, H. Dong, Construction of high-dispersed Ag/Fe_3O_4/g-C_3N_4 photocatalyst by selective photo-deposition and improved photocatalytic activity, Applied Catalysis B: Environmental, 182 (2016) 115-122.

[94] S. Chengjie, F. Mingshan, H. Bo, C. Tianjun, W. Liping, S. Weidong, Synthesis of a g-C_3N_4-sensitized and $NaNbO_3$-substrated II-type heterojunction with enhanced photocatalytic degradation activity, CrystEngComm, 17 (2015) 4575-4583.

[95] M.J. Munoz-Batista, A. Kubacka, M. Fernandez-Garcia, Effect of g-C_3N_4 loading on TiO_2-based photocatalysts: UV and visible degradation of toluene, Catalysis Science & Technology, 4 (2014) 2006-2015.

[96] S. Patnaik, D.P. Sahoo, K. Parida, An overview on Ag modified g-C_3N_4 based nanostructured materials for energy and environmental applications, Renewable and Sustainable Energy Reviews, 82, Part 1 (2018) 1297-1312.

[97] K.S. Lakhi, D.H. Park, K. Al-Bahily, W. Cha, B. Viswanathan, J.H. Choy, A. Vinu, Mesoporous carbon nitrides: Synthesis, functionalization, and applications, Chemical Society Reviews, 46 (2017) 72-101.

Appendix A. g-C_3N_4 based heterostructures for the degradation of organic compounds.

Table A1. Photocatalytic degradation of organic compounds using g-C_3N_4 based heterostructures.

Pollutant	Material combined with g-C_3N_4	Synthesis methods	Removal efficiency (time)	Reference
Acetaldehyde	TiO_2	Wet chemical	100 % (240 min)	[67, 68]
	WO_3	Calcination; mixing-calcination	100 % (24 h)	[67, 69]
Bisphenol A	$Bi_4O_5I_2$	*In situ* growth and solvothermal	90 % (20 min)	[70, 71]
	Co_3O_4	Hard templating-impregnation	93.6 % (180 min)	[67, 72]
Chloramphenicol	$SrFeO_{3-x}$	Sintering	91.3 % (96 h)	[67, 73]
4-Chlorophenol	N-$SrTiO_3$	Thermal exfoliation	(60 min)	[74, 75]
	WO_3	Calcination	43 % (360 min)	[69, 70]
Ciprofloxacin	TiO_2	Solvothermal	97.3 % (150 min)	[67, 76]
Mercaptobenzothiazole	Fe_3O_4	Ultrasonic wet chemistry	85 % (60 min)	[70, 77]
4-Nitroaniline	P-$ZnLn_2S_4$	Solvothermal	99.4 % (90 min)	[67, 78]
Nitrobenzene	$NiTiO_3$	Calcination	80 % (120 min)	[67, 79]
***p*-Nitrophenol**	Ag	Deposition	98 % (120 min)	[74, 80]

	Na-$DyVO_4$	*In situ* ultrasonicated self-assembly	(360 min)	[74, 81]
Phenol	Ag_2O	Liquid phase synthesis	(180 min)	[74, 82]
	C_{60}	Ball-milling	(180 min)	[74, 83]
	$Cd_{0.2}Zn_{0.8}S$	Hydrothermal	76.1 % (180 min)	[67, 84]
	K	Thermal polymerization	(240 min)	[85, 86]
	SnO_{2-x}	Calcination	40 % (90 min)	[67, 87]
	SnS_2	Ultrasonic dispersion	31.3 % (120 min)	[67, 88]
	TiO_2	Solvothermal; hydrothermal	100 % (50 min); (80 min)	[67, 89, 90]
	TiO_2-CdS	Dispersion	(300 min)	[74, 91]
	$ZnIn_2S_4$	Hydrothermal	73.2 % (240 min)	[67, 92]
Tetracycline	Ag/Fe_3O_4	Photodeposition	88 % (90 min)	[67, 93]
	$NaNbO_3$	Solid phase calcination	73.3 % (180 min)	[67, 94]
Toluene	TiO_2	Wet impregnation	*2.0×10^{-10} mol s^{-1} m^{-2}	[67, 95]

*reaction rate constant

Table A2. g-C_3N_4 based photocatalytic degradation of dyes.

Pollutant	Material combined with g-C_3N_4	Synthesis method	Removal efficiency (%) or rate (min^{-1}) (and completion time)	Ref.
Acid Orange 7	TiO_2	Calcination	100 % (300 min)	[67]
Crystal Violet	$SrFeO_{3-x}$	Sintering	99.9 % (12 h)	[67]
Fuchsin	WO_3	-	(60 min)	[74]
Methyl Blue	Ag-based	Photochemical reduction; precipitation; solvothermal	98.9 % (20 min); 97.5 % (60 min); 78 % (360 min); (120 min)	[67, 74, 96]
	Bi-based	Solvothermal; ultrasonication-chemisorption; ultrasonic dispersion	0.0113 min^{-1}; 0.0814 min^{-1}; 0.4701 min^{-1}	[70]
	C_{60}	-	(180 min)	[74]
	CeO_2	Hydrothermal	99 % (210 min); (210 min)	[67, 74]
	Cu	Thermal condensation	100 % (15 min)	[85]
	Eu	Thermal condensation	0.0121 min^{-1}	[85]
	NiO	Calcination	100 % (40 min)	[67]
	$SnNb_2O_6$	Wet chemistry	99 % (240 min)	[67]
	TiO_2-based	Calcination; hydrothermal	92 % (160 min); 89 % (60 min)	[67]
	WO_3	Calcination	97 % (120 min); (60 min)	[70, 74]

	Zn-based	Evaporation-calcination; ultrasonic *in situ* precipitation	78.6 % (120 min); 93%; (150 min); (120 min)	[67, 70, 74]
Methyl Orange	Ag-based	*In situ* oxidation; heating; hydrothermal; liquid phase reaction; ultrasonication/precipitation-deposition	72.6 % (60 min); 78.9 % (120 min); 100 % (120 min); 90 % (210 min); 96.5 % (50 min); (120 min); (30 min); (30 min)	[67, 74, 96]
	Au	-	(150 min)	[74]
	$BaTiO_3$	Mixing-calcination	76 % (360 min)	[67]
	Bi_2WO_6	Calcination	0.0365 min^{-1}; (120 min)	[70, 74]
	C	-	(240 min)	[74]
	CdS	-	(16 min)	[74]
	CeO_2-based	Mixing-calcination; mixing-calcination	74 % (120 min); 0.011 min^{-1}	[67, 96]
	$Cr/SrTiO_3$	Mixing-calcination	100 % (240 min)	[67]
	Cu	Thermal condensation	90.2% (60 min)	[85]
	$MnFe_2O_4$	Chemical impregnation	99.3% (180 min)	[70]
	$NaNbO_3$	Solid phase calcination	77.2 % (180 min)	[67]
	Sb_2S_3	-	0.0103 min^{-1}	[96]
	SnO_2	Mixing-calcination; ultrasonic dispersion	73 % (180 min); 95 % (40 min); (180 min)	[67, 74]
	SnS_2	Ion-exchange	95.3 % (25 min)	[67]

	TiO_2	Calcination; electrochemical	55 % (180 min); 100 % (150 min); (50 min); (80 min)	[67, 74]
	W	Hydrothermal	0.0627 min^{-1}	[85]
	Zn-based	Hydrothermal; hydrothermal; solvothermal	95.3 % (120 min); 93% (100 min); 98 % (180 min)	[67, 70]
Orange II	$CuFe_2O_4$	Self-assembly	98 % (180 min)	[70]
Rhodamine B	Ag-based	Calcination; chemical adsorption; chemical reduction; chemical precipitation; co-precipitation; co-precipitation; *in situ* ion exchange; *in situ* thermal condensation; ion impregnation; hydrothermal; photoreduction; precipitation; solvothermal	95.0 % (90 min); 100 % (50 min); 80% (180 min); 100 % (40 min); 75.0 % (60 min); 90.0 %; 100 % (30 min); 98.6 % (60 min); 96 % (20 min); 41.2 % (30 min); 90 % (20 min); 100 % (25 min); 98.6 % (60 min)	[67, 74, 96]
	Al_2O_3	Ultrasonic dispersion	0.0257 min^{-1}	[70]
	Au-C	-	(50 min)	[74]
	B	Co-polycondensation	0.199 min^{-1}	[85]
	Bi-based	*In situ* growth; i*n situ* growth and solvothermal; solvothermal; ultrasonic dispersion	0.3608 min^{-1}; 70 % (60 min); 98 % (70 min); 94.4 % (15 min); (50 min)	[67, 70, 74]
	C-based	Polycondensation	0.0362 min^{-1}; (60 min)	[74, 85]
	$Cd_{0.2}Zn_{0.8}S$	Hydrothermal	95.8 % (80 min)	[67]

Ce	Annealing	0.0155 min^{-1}	[85]
CeO_2/N-rGO	Ultrasonic-heating	0.025 min^{-1}	[70]
$DyVO_4$	Milling and heating	0.0365 min^{-1}	[70]
Fe-based	Thermal condensation	99.5 % (120 min); (90 min)	[74, 85]
$GdVO_4$	Milling and heating	96.7 % (90 min)	[67]
$HSbO_3$	Heating; mixing-calcination	100 % (360 min); 90 % (240 min)	[67, 70]
HWO_4	Impregnation	81.3 % (50 min)	[67]
In_2S_3	Hydrothermal	96 % (30 min)	[67, 70]
K	Annealing	0.011 min−1	[85]
Na-based	Solid phase calcination; thermal polymerization; ultrasonic dispersion	93.6 % (120 min); 0.0064 min^{-1}; 90 % (180 min); (80 min)	[67, 70, 74, 85]
P	Co-polycondensation; co-polycondensation; co-polycondensation	98 % (60 min); 0.0466 min^{-1}; 0.09856 min^{-1}	[85, 97]
S	Co-polycondensation	0.0167 min^{-1}	[85]
SiO_2	Calcination; heating; mixing-calcination	99.9 % and 0.051 min^{-1} (90 min); 94 %; 94.3 % (150 min)	[67, 70]
SnS_2	Ultrasonic dispersion	99.8 % (20 min)	[67]
$SmVO_4$	Mixing-calcination	0.0345 min^{-1}	[70]
$SrTiO_3$-N	-	60 min	[74]

	TiO_2-based	Hard templating; hydrothermal-sonication; self-assembly; solvothermal	96.5 % (100 min); 97 % (120 min); 82 % (80 min); 99.3 % (150 min); (300 min)	[67, 74]
	V_2O_5	*In situ* growth	95.5 % (60 min)	[67]
	WO_3	Mixing-calcination	91 % (90 min); (120 min)	[67, 74]
	Y	Thermal condensation	100 % (110 min)	[85]
	Zn-based	Anion exchange; calcination-hydrothermal; coprecipitation and calcination; deposition-precipitation and thermal; hydrothermal; sonochemical impregnation	100 % (75 min); 97.9 % (90 min); 99 % (15 min); 0.0367 min^{-1}; 98 % (90 min); 100 % (60 min); (60 min)	[67, 70, 74]
	Zr	Thermal condensation	100 % (110 min)	[85]
Sulforhodamine B	TiO_2	Solvent evaporation	56.3 % (300 min)	[67]

Appendix B. Scheme of gCN preparation.

Figure B1 represents the sequential thermal conversion of dicyandiamide to melamine, melem, melon and polymeric g-C_3N_4 (gCN).

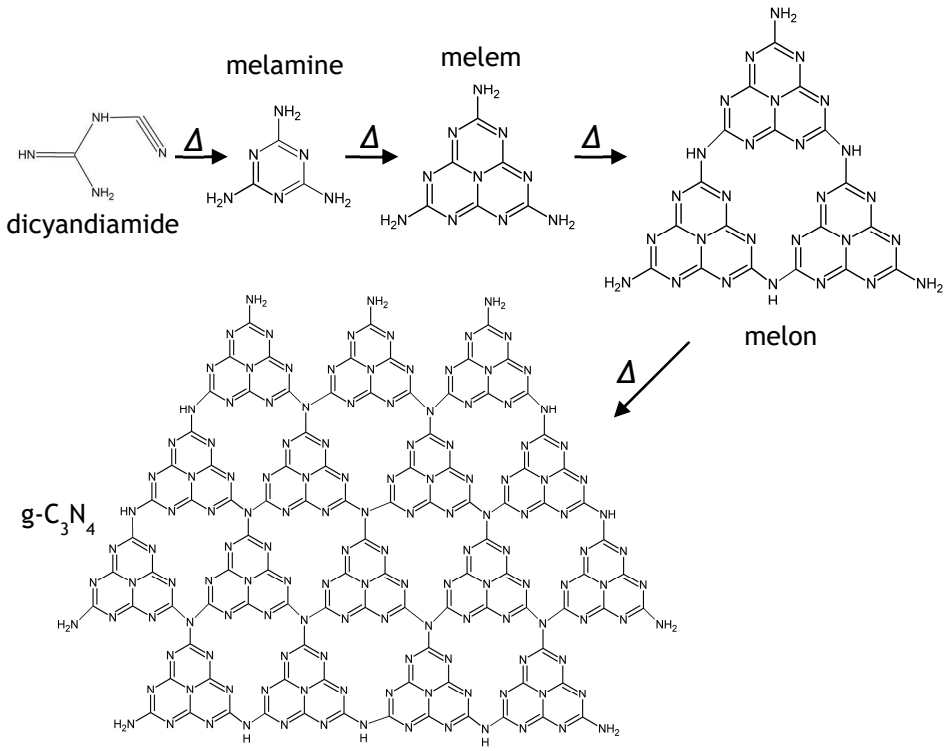

Figure B1. Production of gCN: sequential thermal conversion of dicyandiamide to melamine, melem, melon and polymeric g-C_3N_4.

Appendix C. UV-Vis spectra of selected compounds.

Figure C1 shows the emission spectrum of the LEDs used in the photocatalytic experiments and the UV-Vis absorbance spectrum of phenol.

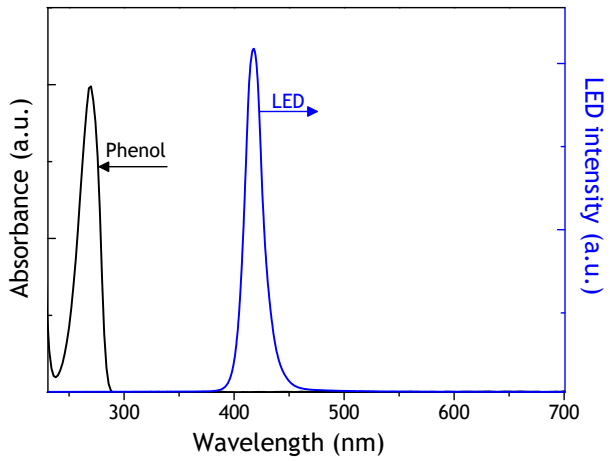

Figure C1. Spectra of phenol UV-Vis absorbance and LED emission.

UV-vis spectra were recorded for all the studied compounds (Figure C2). The wavelengths at the maximum absorbance (λ_{max}) are listed in Table C1.

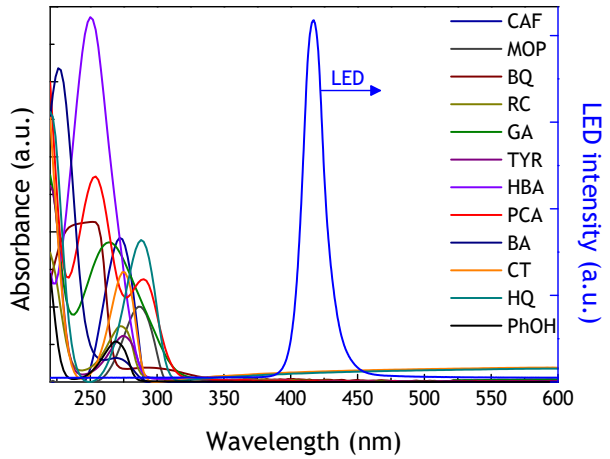

Figure C2. UV-Vis spectra of aromatic compounds and LED emission spectra.

Table C1. Wavelength at maximum absorbance of aromatic compounds.

Compound	λ_{max} (nm)
Phenol	270
Catechol	274
Resorcinol	272
Hydroquinone	288
Benzoic acid	270
4-Hydroxybenzoic acid	250
Protocatechuic acid	290
Gallic acid	264
4-Methoxyphenol	286
Tyrosol	274
Caffeine	272
Benzoquinone	252